JOURNAL OF GEOPHYSICAL RESEARCH, VOL. 113, E12S38, doi:10.1029/2008JE003237, 2008

Rock spectral classes observed by the Spirit Rover's Pancam on the Gusev Crater Plains and in the Columbia Hills

W. H. Farrand,[1] J. F. Bell III,[2] J. R. Johnson,[3] R. E. Arvidson,[4] L. S. Crumpler,[5] J. A. Hurowitz,[6] and C. Schröder[7]

Received 8 July 2008; accepted 17 September 2008; published 16 December 2008.

[1] This paper examines the ferrous and ferric iron mineralogy of rocks inferred from 246 visible/near-infrared (430–1010 nm) multispectral observations made by the Mars Exploration Rover Spirit's Pancam on its traverse from its landing site to its second Winter Haven location. Principal component, correspondence analyses, and a sequential maximum angle convex cone technique were used to identify 14 candidate classes. Spectra from the West Spur of Husband Hill and the Watchtower area had the highest 535 and 601 nm band depths indicating that these areas were more oxidized. Differences in the depth and band center of a near infrared (NIR) absorption feature were observed using 904 nm band depth and 803:904 nm ratio and parameters gauging the 754–864 and 754–1009 nm slopes. Spectra of rocks from the southern flank of Husband Hill had negative 754–1009 nm slopes and a broad NIR absorption consistent with high olivine abundances. Rocks observed on the lower West Spur, at the Cumberland Ridge locale, at the Husband Hill summit, and at the Haskin Ridge locale had deep 904 nm band depths and steep 754–864 nm slopes consistent with greater pyroxene abundances. These observations are consistent with results on iron-bearing mineralogy from Spirit's Mössbauer spectrometer. Comparisons of these rock spectral classes with a set of terrestrial analog samples found similarities between the West Spur and Watchtower classes and red hematite-bearing impact melts. Fewer similarities were found in comparisons of the Columbia Hills classes with basaltic hydrovolcanic tephras.

Citation: Farrand, W. H., J. F. Bell III, J. R. Johnson, R. E. Arvidson, L. S. Crumpler, J. A. Hurowitz, and C. Schröder (2008), Rock spectral classes observed by the Spirit Rover's Pancam on the Gusev Crater Plains and in the Columbia Hills, *J. Geophys. Res.*, *113*, E12S38, doi:10.1029/2008JE003237.

1. Introduction

[2] In the time from its landing to its second Martian winter, the Mars Exploration Rover Spirit traversed 2 km from its landing site on the plains of Gusev Crater to the Columbia Hills and explored the eastern and southern flanks of Husband Hill, and the "Inner Basin" south of Husband Hill [*Arvidson et al.*, 2006, 2008]. During these journeys, the rover encountered a number of rock types that in situ analysis has shown to be distinct in chemistry and iron-bearing mineralogy [*McSween et al.*, 2006a, 2006b; *Ming et al.*, 2006, 2008; *Morris et al.*, 2006, 2008; *Squyres et al.*, 2006] as well as in their thermal infrared emittance spectra [*Ruff et al.*, 2006]. An earlier paper detailed multispectral Visible and Near Infrared (VNIR) differences observed among rocks encountered through sol 419 of Spirit's mission [*Farrand et al.*, 2006]. This paper broadens those spectral classes to encompass all those rocks examined up to Spirit's second Winter Haven sojourn (up to approximately sol 800) and examines their distinguishing characteristics for comparison to other measurements made with Spirit's Athena science package [*Squyres et al.*, 2003]. Figure 1 shows Spirit's traverse path over Husband Hill and to Home Plate and includes names of prominent rocks mentioned in this paper.

[3] The Athena science package includes the Alpha Particle X-Ray Spectrometer (APXS), which provides information on elemental chemistry, the Mössbauer (MB) spectrometer which provides information on iron mineralogy, the Microscopic Imager (MI) which provides information on the fine-scale morphology, grain size, and textures, and the Miniature Thermal Emission Spectrometer (Mini-TES) which provides information on mineralogy. The multispectral Pancam data are used to support mineralogic assignments made using data from these other instruments. For example, multispectral Pancam data provide information in conjunction with MB data to help assess the role that

[1]Space Science Institute, Boulder, Colorado, USA.
[2]Department of Astronomy, Cornell University, Ithaca, New York, USA.
[3]Astrogeology Team, U.S. Geological Survey, Flagstaff, Arizona, USA.
[4]Department of Earth and Planetary Sciences, Washington University, St. Louis, Missouri, USA.
[5]New Mexico Museum of Natural History and Science, Albuquerque, New Mexico, USA.
[6]Jet Propulsion Laboratory, Pasadena, California, USA.
[7]NASA Johnson Space Center, Houston, Texas, USA.

0148-0227/08/2008JE003237$09.00

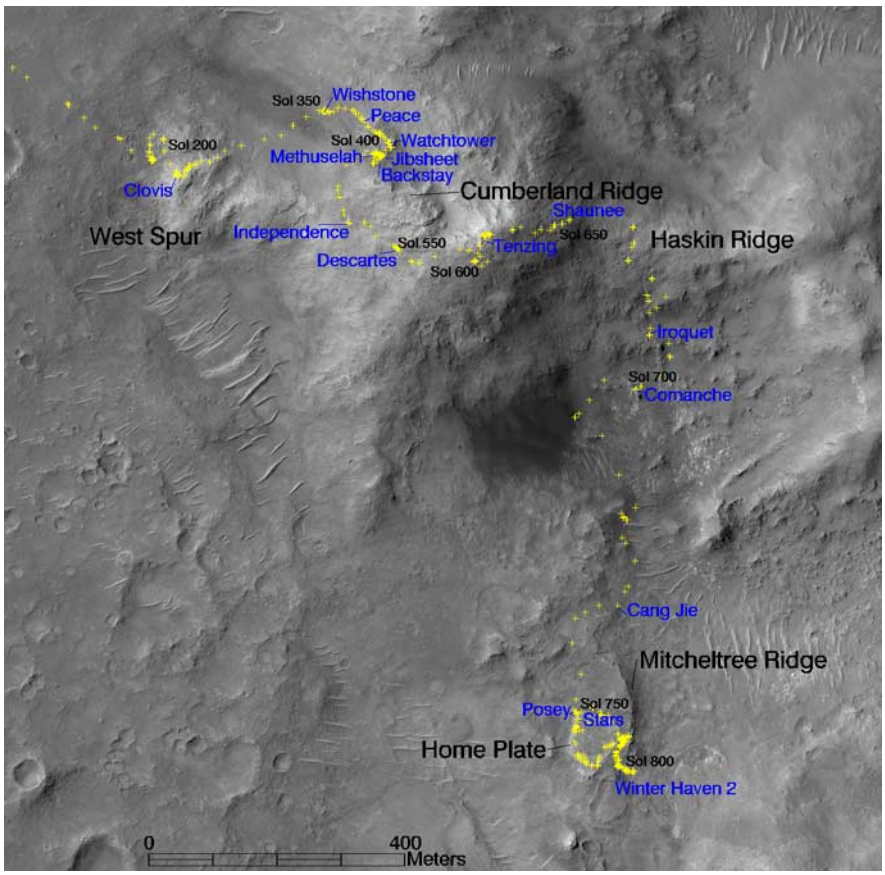

Figure 1. Spirit's traverse (yellow crosses) overlain on orbital HiRISE image. Landmark topographic features and representative sol numbers are provided in black. Also a number of significant rocks mentioned in the text are labeled in blue.

ferric iron plays in contributing to the VNIR reflectance. The color Pancam data are often taken in conjunction with Mini-TES point spectra to provide context for the Mini-TES targets with other nearby materials. Finally, Pancam measurements can be used to place into context measurements made by orbital instruments such as the Mars Express High Resolution Stereo Camera (HRSC) and Observatoire pour la Minéralogie l'eau les Glaces et L'Atmosphére (OMEGA) and/or the Mars Reconnaissance Orbiter Compact Reconnaissance Imaging Spectrometer for Mars (CRISM) and High-Resolution Imaging Science Experiment (HiRISE).

2. Pancam Instrument

[4] A detailed description of the Pancam instrument and preflight calibration are given by *Bell et al.* [2003]. Information on the ongoing operation of Pancam and calibration of Pancam data is provided by *Bell et al.* [2006]. In brief, the Pancam has two 1024 rows by 1024 columns of charge-coupled devices (CCDs) with a 30 cm stereo separation and a 0.27 mrad per pixel resolution. The Pancam is mounted 1.5 m above the ground on a mast (the Pancam mast assembly, or PMA). Each camera has an eight-position filter wheel. One filter position (the *L*1 band) is a broad band unfiltered channel, used for albedo panoramas [*Bell et al.*, 2008]. There are also two neutral density filters (the *L*8 and *R*8 bands) for solar observations. This leaves 13 filters covering 11 unique VNIR wavelengths for multispectral geologic investigations with the near-UV to visible filters in the left eye and the visible to near-IR filters in the right eye. Table 1 lists the left- and right-eye band names, centers, and Full Width at Half Maximum (FWHM) values of the 13 "geology" bands.

3. Data Reduction and Processing

[5] The Pancam was calibrated before launch as described by *Bell et al.* [2003; 2006]. With the acquisition of each multispectral data set, a calibration target was also imaged close in time to the observation. The calibration target (described by *Bell et al.* [2003, 2006]) has four color chips, multiple gray rings and a post that casts a shadow across the gray rings, allowing for estimation of diffuse illumination. Multispectral image data from the calibration target, in conjunction with prelaunch calibration information, were used to convert raw image data to calibrated radiance and then to the radiance factor I/F (where I is the measured radiance and πF is the incident solar irradiance). Accumulation of air fall dust on the calibration target over the course of the mission was compensated through the use of a two-layer Hapke model along with the known photometric properties of the calibration target [*Bell et al.*, 2006; *Sohl-Dickstein et al.*, 2005; *Kinch et al.*, 2007].

Table 1. Pancam Band Names, Centers, and FWHM Widths

Band	Center (nm)	FWHM Width (nm)
*L*7	432	25
*L*6	482	27
*L*5	535	19
*L*4	601	17
*L*3	673	16
*L*2	753	20
*R*1	436	25
*R*2	754	19
*R*3	803	20
*R*4	864	17
*R*5	904	25
*R*6	934	24
*R*7	1009	28

[6] The solar incidence angle recorded for each scene was used to convert the data to relative reflectance (*R**, defined as *I*/*F* divided by the cosine of the incidence angle [*Reid et al.*, 1999; *Bell et al.*, 2006]). *Bell et al.* [2006] estimated the absolute reflectance levels of these data to be accurate to within ~10% at the shortest wavelengths, and probably slightly more accurate at longer wavelengths. Relative filter-to-filter uncertainties in *R** were estimated to be typically 1–5%, providing confidence in the reality of even very small-scale spectral variations detected in a given scene. Data transmitted to Earth were first subjected to a wavelet-based compression onboard the spacecraft. The 13-filter data sets examined here were collected at 12 bits and then companded to 8-bit data using an approximate square root lookup table and then typically compressed so that blue stereo bands (the *L*7 and *R*1 bands) were at 2 bits/pixel and all other bands were at 1 bit/pixel (corresponding to effective compression ratios of 8:1 and 16:1, respectively). Some of the scenes considered here had lower compression levels. The effects of compression on radiometric precision were estimated to be <1% on the basis of prelaunch tests [*Bell et al.*, 2006].

[7] As is discussed below, the techniques utilized to discriminate spectral classes were applied to the full range of Pancam multispectral data. These consisted of averages of spectra from regions of interest (ROIs) on rock surfaces that were either brushed or abraded by the rover's Rock Abrasion Tool (RAT) or that were swept relatively clean by eolian erosion. The number of pixels used for these ROIs varied from as few as five pixels to forty or more. Because Pancam is a stereo camera and divides the spectral range between the two "eyes" of the camera, the full spectral range is not immediately accessible. However, once common areas on rock surfaces are identified, spectra can be extracted from each "eye" and joined at the overlap area at 753–754 nm (shorter-wavelength channels additively increased by the amount required for the reflectance at the 753 nm band to match that at the 754 nm band). A set of 246 combined eye spectra of representative rocks was assembled and considered in this analysis. The *R*1 band, centered at 436 nm, was excluded from the analysis because it was generally redundant with the *L*7 band centered at 432 nm. The resulting set of 12 band spectra were assembled in a spreadsheet and consequently utilized as if it were a "spectral slice, "i.e., a two dimensional data set one sample wide, 246 lines long and 12 bands deep. This product was used for the subsequent spectral class determinations described below.

4. Derivation of Spectral Classes

4.1. Background

[8] *Farrand et al.* [2006] utilized spectral mixture analysis (SMA) to assess the spectral variability of rocks examined by Spirit through sol 419. In that earlier work, numerous 13 filter scenes were modeled using SMA (using the implementation described by *Adams et al.* [1993]) in order to determine regions of interest most representative of rock surfaces and to search for spectral variability in the scenes. Some scenes were found to have more than one spectral rock type in them. VNIR spectral classes were determined through examination of spectral parameters from regions of interest on rock surfaces that were determined through the SMA.

[9] In this paper, several procedures for determining "end-member" spectra were utilized to determine spectrally unique classes observed on Spirit's traverse. These procedures included principal components analysis (PCA) [e.g., *Davis*, 1973; *Singh and Harrison*, 1985], correspondence analysis (CA) [*Davis*, 1973; *Tian et al.*, 1993; *Larsen et al.*, 2000] and a Sequential Maximum Angle Convex Cone (SMACC) approach [*Gruninger et al.*, 2004]. After determining a set of candidate spectral classes, a subset of the 246 spectra database was examined using plots of spectral parameters to better understand the underlying spectral characteristics that made these classes unique.

[10] The VNIR spectral range covered by the Pancam is most sensitive to iron-bearing mineralogy. A full discussion of this topic is beyond the scope of this paper, but is reviewed in numerous sources [e.g., *Burns*, 1970, 1993; *Gaffey et al.*, 1993; *Morris et al.*, 1985]. However, in brief, the spectral range considered here is affected by several effects involving the iron cation. These include an intense Fe^{3+}–O^{2-} charge transfer that greatly reduces reflectance from below 550 nm into the ultraviolet and absorption features caused by crystal field transitions in the Fe^{3+} or Fe^{2+} cation. For example, in hematite the absorption band centered near 860 nm and the shoulder centered near 630 nm are the result of the ${}^6A_1 \rightarrow {}^4T_1$ and ${}^6A_1 \rightarrow {}^4T_2$ transitions respectively [*Morris et al.*, 1985]. In ferrous-iron-bearing phases, principally olivine and pyroxenes, there is an absorption feature in the 900–1250 nm region. In olivine this is due to an amalgam of three bands centered near 900, 1060, and 1250 nm caused by transitions related to the positioning of the Fe^{2+} cation in the *M*1 and *M*2 sites of the olivine crystal [*Burns*, 1993]. In pyroxene, low-Ca pyroxenes have a crystal field band centered near 900 nm caused by Fe^{2+} in the *M*2 site in the more Ca-rich pyroxenes this absorption feature is shifted to longer wavelengths centered near 1030 nm [*Burns*, 1993]. The strength and positioning of these absorption features influence the shape of the resulting spectrum and consequently affect the values of the spectral parameters used in this analysis and described below in section 4.5.

4.2. Principal Components Analysis

[11] Since the rock spectra observed by Spirit are, to first order, similar and highly correlated, using an approach such

Table 2. Description of Spectral Parameters Used in This Study

Parameter	Description	Related Characteristic
535 nm band depth	$1 - (R^*_{535} / [(0.570R^*_{432}) + (0.430R^*_{673})])$	Degree of oxidation and can represent incipient hematite development
482–673 nm slope	$(R^*_{673} - R^*_{482}) / (673 - 482)$	Degree of oxidation
601 nm band depth	$1 - (R^*_{601} / [(0.522R^*_{535}) + (0.478R^*_{673})])$	Can be affected by goethite development and can be influenced by olivine versus pyroxene
904 nm band depth	$1 - (R^*_{904} / [(0.510R^*_{803}) + (0.43R^*_{1009})])$	Strength of NIR absorption
803:904 nm ratio	$R3:R5$ (803:904 nm band)	Strength of NIR absorption
754–864 nm slope	$(R^*_{754} - R^*_{864}) / (864 - 754)$	Strength and position of NIR absorption
754–1009 nm slope	$(R^*_{754} - R^*_{1009}) / (1009 - 754)$	Strength and position of NIR absorption

as principal components, which maximizes variance, is appropriate to separate the observations into spectral classes. PCA is an orthogonal linear transformation that transforms the given data set into a new coordinate space where the greatest variance lies along the first coordinate (or first principal component (PC1)), the second greatest variance lies along the PC2, the third greatest along the third and so forth. After subjecting the 246 rock spectra to a principal components transformation, the resulting breakdown of variance was such that 94.896% of the variance was in the first component, 3.765 in the second, 0.812 in the third, 0.215 in the fourth and 0.166 in the fifth with the remainder each having less than 0.1% of the variance. As discussed below, the components were plotted against each other in order to find those samples at the extremes of the resulting data cloud.

4.3. Correspondence Analysis

[12] Correspondence Analysis (CA) [e.g., *Tian et al.*, 1993; *Larsen et al.*, 2000] is a related approach to PCA but it scales the data in order to treat the variables (in this case, wavelength) and samples (in this case, spectra) equivalently. Thus in CA, the principal factors in variable space contribute the same to the total variation as do the principal factors in sample space. Consequently, the transformed variables and samples can be plotted together in factor space. Variables that plot near each other are more highly correlated than those that plot further away. Similarly, samples that plot near each other are more highly correlated than samples that plot far from each other. Correlation between one or more samples and one or more variables is evidenced in the combined plot of variables and samples when those samples plot near a variable or set of variables. In the present case, use of CA allows us to better relate the connection between samples that plot at the extreme positions in factor space with wavelength so that underlying causes (such as absorption bands at specific wavelength positions) of the spectral variation can be better understood.

4.4. Sequential Maximum Angle Convex Cone

[13] An automatic tool that replicates some of the functionality of PCA in terms of finding spectrally extreme, or end-member, spectra is the Sequential Maximum Angle Convex Cone algorithm [*Gruninger et al.*, 2004; ITT Visual Information Solutions, Environment for Visualizing Images version 4.4 (ENVI 4.4), 2007]. SMACC first finds the pixel in the image with the highest overall albedo, then it finds the pixel most different from the brightest, which can be the lowest-albedo sample. Then, it finds the pixel most different from the first two. The process is repeated until SMACC finds a pixel already accounted for in the group of the previously found pixels, or until it finds a specified number of end-members. The drawback of this method is that it finds single pixel end-members and the pixel most unlike other pixels is often one that is affected by noise and is thus unrepresentative of actual materials. Therefore, when running the SMACC algorithm one sets a number of end-members larger than that actually expected so that spurious single pixels might be excluded. SMACC was run on the 246 combined eye spectra as described above. The overall reflectance, or albedo, of the spectra can influence end-member selection in SMACC. In order to ensure that albedo was not overly influencing the selection of end-members, SMACC was run on both the R^* data and on an albedo-normalized version of the data produced by application of a hyperspherical directional cosine transformation [*Pouch and Campagna*, 1990] of the R^* data. With the unnormalized data the first end-member selected is the one with the highest overall reflectance and may or may not be a spectrum representative of any meaningful class.

4.5. Examination of Spectral Parameters

[14] *Farrand et al.* [2006] examined spectral parameters of rock spectra collected up to sol 419 and, based primarily on groupings observed within plots of spectral parameters, established a set of six spectral classes. Given the larger number of spectra available for this study, a somewhat different methodology was followed. Through the techniques discussed above, 14 candidate spectral classes were identified. A set of spectral parameters, listed and defined in Table 2, were used and representative spectra of the candidate classes were examined to determine which, if any, had extreme values in these parameters. The spectra used for the parameter plots discussed in section 5.5 are those that had these extreme values. The spectral parameters used included those that provided measures of the character of the ferric absorption edge (535 nm band depth, blue to red slope, and, 601 nm band depth). These parameters can also be used to help distinguish between ferric oxide phases as demonstrated by *Morris et al.* [2000]. The strength of the NIR absorption at 900–1009 nm and/or other effects contributing to the continuum or slope from 754 to 1009 nm were examined using the parameters of 904 nm band depth, ratio of $R3$ over $R5$ (803:904 nm), slope from 754 to 864 nm, and slope from 754 to 1009 nm.

4.6. Tools for Intercomparison of Spectra

[15] As is described below, a set of candidate spectral classes were determined through application of PCA, CA,

Table 3. Candidate Spectral Classes Compared to APXS Rock Classes

Candidate Class	Representative Spectra With Sol Number and Pancam Sequence Identifier	APXS Rock Class Names	Type APXS Analyses[a]
Plains Basalts	A54 Humphrey undisturbed p2429	Adirondack class[b]	A34 Adirondack_RAT
West Spur	A227 Frio P2571	Clovis class[b]	A218 Clovis_Plano_RAT
Wishstone	A343 LaBrea P2574	Wishstone class[b]	A335 Wishstone_Chisel_RAT
Peace	A381 Peace RAT P2543	Peace class[b]	A380 Peace_RAT2
Watchtower	A419 Watchtower P2574	Watchtower class[b]	A417 Watchtower_Joker_RAT
Methuselah	A608 Bowline P2582	Watchtower class[b]	A417 Watchtower_Joker_RAT
Jibsheet	A487 Davis P2531	Watchtower class[b]	A417 Watchtower_Joker_RAT
Backstay	A511 Backstay P2553	Backstay class[b]	A511 Backstay_Scuppers
Independence	A536 Independence P2540	Independence class[c]	NA
Descartes	A551 Descartes P2558	Descartes class[c]	NA
Seminole	A689 Wolf Lake p2568	Algonquin class[c]	NA
Comanche	A695 Comanche p2584	Algonquin class[c]	NA
Posey	A753 Posey RAT brushed P2583	Barnhill class[c]	NA
Stars	A764 Stars p2589	Barnhill class[c]	NA

[a]APXS spectra names and sol numbers from *Gellert et al.* [2006].
[b]Rock class designations from *Squyres et al.* [2006].
[c]Rock class designations from *McSween et al.* [2008] are informal and are the subject of an upcoming publication that will formally define rock class names, type spectra, and analyzed rocks that fall into each designated class.

SMACC, visual examination of spectra, and examination of spectral parameter plots. The PCA, CA, and SMACC analyses produced one to several spectra deemed most representative of each candidate class. Visual inspection of spectra provided other candidate spectra. To determine which one or two spectra might be the most representative of each candidate class, two to five spectra for each class were intercompared using a root mean square metric and a spectral angle comparison with these comparison tools contained in a spectral library analysis tool set [*Dennison et al.*, 2004]. Root mean square or RMS error ε is defined by

$$\varepsilon = \left[M^{-1} \sum_{c=1} n_c^2 \right]^{1/2},$$

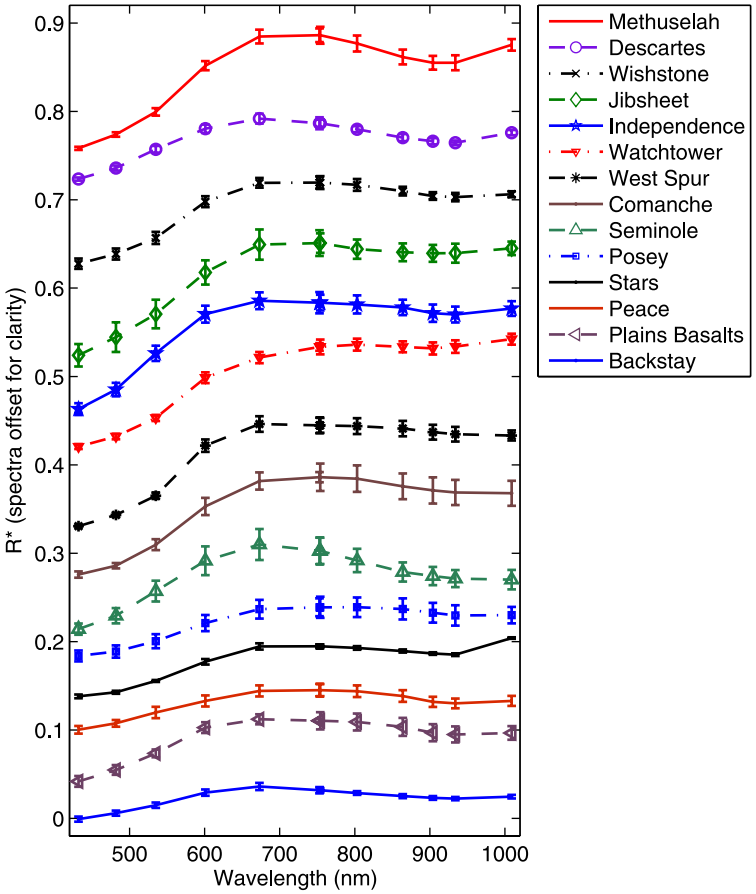

Figure 2. Representative spectra of 14 candidate spectral classes. Error bars here, and in Figures 13, 14, 16, and 18, represent standard deviation of the mean of pixels averaged for the spectra. Observations from which these spectra are drawn are listed in Table 3.

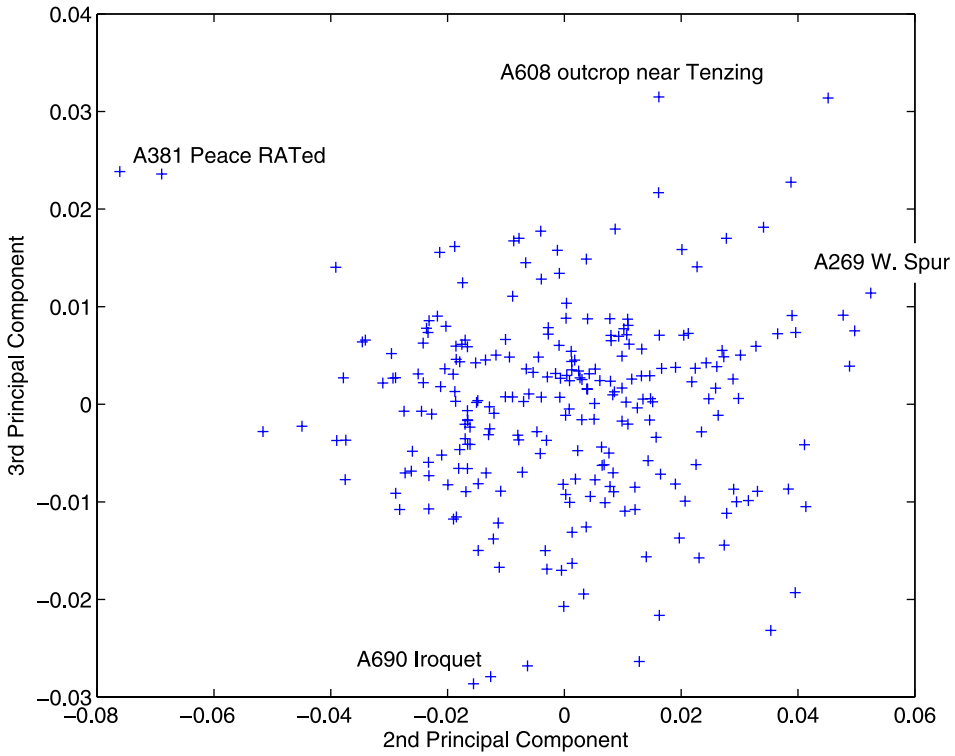

Figure 3. Example plot of second versus third principal component for 246 spectra database with minimum and maximum points annotated.

where ε is the RMS error, M is the number of channels, c is channel number, and n is the vector of residuals between the modeled and the measured relative reflectances. The spectral angle metric is essentially the application of a cosine dot product to two spectra. A low spectral angle value (in radians) indicates that the two spectra are similar.

5. Results

5.1. Candidate Classes

[16] The results of the analysis techniques outlined above were the 14 candidate classes listed in Table 3 and shown in Figure 2. Table 3 lists the candidate classes and provides the name of a spectrum representative of that candidate class. Also shown on Table 3 are rock classes defined by the APXS instrument, along with the name of the type APXS spectra, and the sol on which it was collected. In the following sections, we discuss how these classes were derived and then examine their unique spectral characteristics using spectral parameter plots. Note that the classes defined here are based solely on spectral characteristics. Thus, while there are in some instances correspondence with the rock classes defined on the basis of chemical composition by *McSween et al.* [2006a, 2006b], *Ming et al.* [2006, 2008], *Morris et al.* [2006, 2008], and *Squyres et al.* [2006] in other instances there are significant differences. For example, plains basalts such as Humphrey have spectral characteristics which are highly similar to those of vesicular basalts such as Masada although these rocks differ in terms of their chemistry.

5.2. Principal Components Analysis Classes

[17] Figure 3 shows a plot of second versus third principal component with minimum and maximum points labeled. Table 4 shows the results from this plot and from similar plots (not shown here) of the third versus the fourth principal component as well as one of the first versus the second principal component with, from each, the two to three spectra which had either maximum or minimum component values resulting from the PCA analysis. On the basis of these results, the PC1 clearly represents albedo with the minimum component values representing the brightest spectra and the maximum component values

Table 4. Spectra Which Had Maximum and Minimum Component Values Resulting From PCA for the First Four Principal Components

	Minimum	Maximum
PC1	a386 near Alligator p2546, a608 outcrop p2583, and a200 Wooly Patch scuffed p2556	a511 Backstay 1 p2563 and a511 Backstay 2 p2563
PC2	a381 Peace RAT 1 p2543 and a381 Peace RAT 2 p2543	a269 unnamed rock p2534 and a269 Palenque p2534
PC3	a690 Iroquet RAT brushed p2575, a689 Wolf Lake p2568, and a690 Iroquet bare p2575	a608 outcrop 2 p2583, a220 unnamed rock p2565, and a419 Watchtower RATed p2574
PC4	a879 layers p2265, a386 near Alligator p2546, and a269 unnamed rock p2534	a764 Stars RAT brush p2589 and a663 Lovegrass 2 p2532

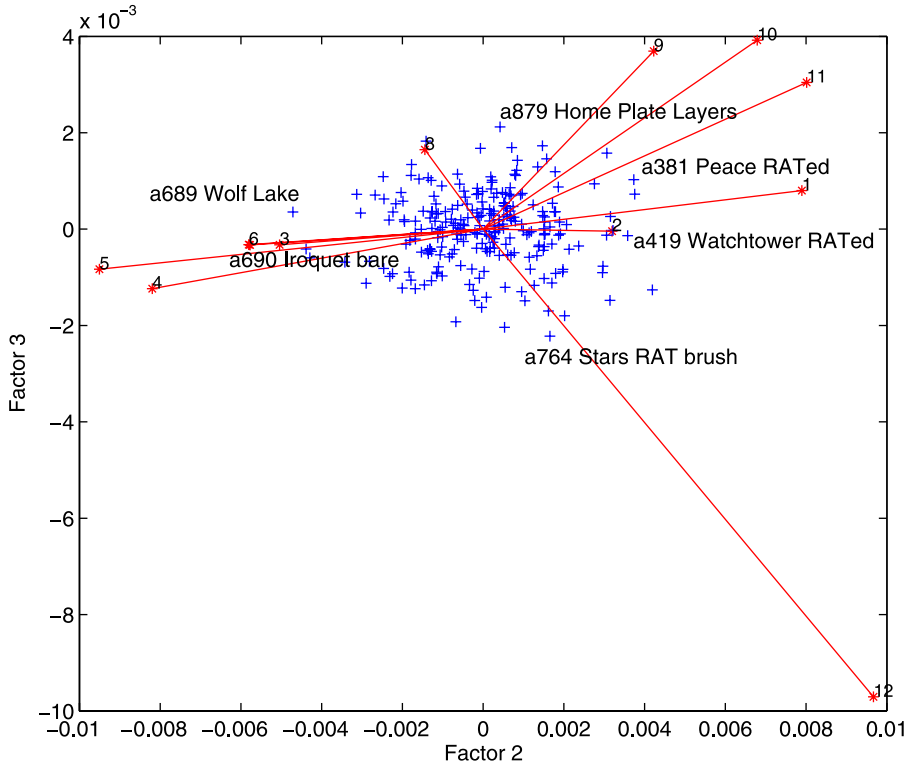

Figure 4. Plot of factor 2 versus factor 3 from correspondence analysis. Here and in Figure 5 blue crosses indicate spectral measurements and red asterisks indicate Pancam spectral bands; here labeled 1–12 (from 432 to 1009 nm) for ease of interpretation.

representing the samples with the lowest reflectance over all Pancam bands. The association of the maximum and minimum PC2 values with spectra that had distinctive character at the shortest wavelengths indicates that PC2 is dictated by the short-wavelength character (e.g., the slope of the blue-to-red spectrum and the presence or absence of a 535 nm inflection in that slope) of the spectra. The maximum component values for PC2 were represented by the West Spur rocks which are highly oxidized (high Fe^{3+}/Fe_{Total} in Mössbauer spectrometer measurements [*Morris et al.*, 2006]) and the minimum component values represented by the Peace RAT measurements, which had a flat to convex blue to red spectral shape. PC3 appears related to the NIR spectral character with the minimum component values represented by the Seminole class, which has a strong NIR absorption and negative 754–1009 nm slope while the maximum component values are represented by the Watchtower class which has a positive 754–1009 nm slope. The meaning of the minimum values of PC4 are ambiguous since the three minimum value spectra seemingly lack distinct common characteristics; however the maximum values of PC4 show the broad NIR absorption with steep, positive slope from 934 to 1009 nm seen in the sol 764 Stars and Crawfords RAT brush measurements and also in the sol 663 (not examined by Instrument Deployment Device (IDD)) Lovegrass rock target.

5.3. Correspondence Analysis

[18] Application of Correspondence Analysis (CA) to the data produced a set of plots such as those shown in Figures 4 and 5. Spectra associated with minimum and maximum values of these factors are listed in Table 5. In Figures 4 and 5, variables (wavelength) are plotted as numbered red asterisks (numbers representing the band number from shortest to longest wavelength) with lines back to the origin and samples (spectral measurements) are plotted as blue crosses. As with PCA, factor 1 (not shown) appears to be most closely associated with albedo. For factor 1, the lowest values are associated with the highest-albedo samples and the highest values are associated with low-albedo samples. Higher factors are more closely associated with spectral features such as the slope of the blue-to-red absorption edge, presence or absence of a 535 nm kink, depth of a NIR absorption band. This is indicated on the basis of the samples at the maximum and minimum values of the first factor versus those associated with higher factors. Samples with maximum and minimum values in the first factor are distinguished primarily on the basis of albedo, those associated with higher values are more closely associated with spectral features, and thus these higher factors are shown in Figures 4 and 5. Figure 4 plots factor 2 versus factor 3. Whereas in the PCA technique the NIR slope was associated with PC3 here it is associated with factor 2. The lowest values of factor 2 are associated with spectra associated with the Seminole class (a negative 754–1009 nm slope). The highest values of factor 2 are associated with Watchtower class spectra (positive 754–1009 nm slope). Given the plotting of both wavelength and samples in CA, we can associate more than just minimum and maximum factor values. The sample most associated with band 12, e.g., *R*7

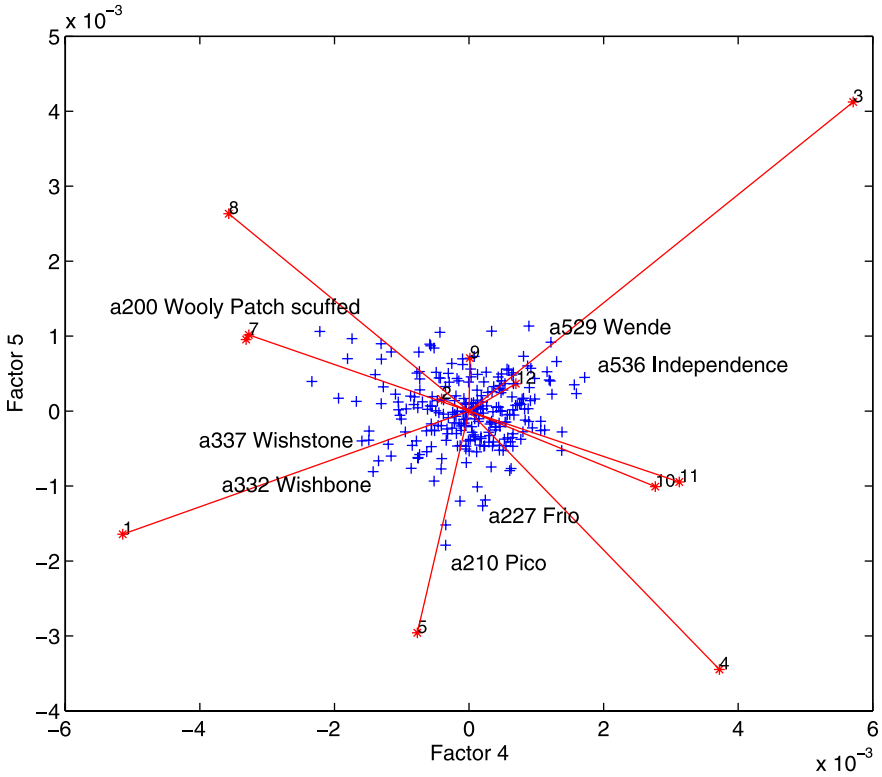

Figure 5. Plot of factor 4 versus factor 5 from correspondence analysis.

(1009 nm), in Figure 4 is the Stars RAT brush measurement which has a high 935–1009 nm slope. This sample also has the lowest factor 3 value. The highest factor 3 values are associated with Posey class spectra which have a weak NIR absorption band. In Figure 5, the maximum values of factor 4 are associated with Independence class spectra, the minimum values of factor 5 are associated with the West Spur class spectra. The West Spur spectra occur near the projections for bands 4 and 5 (*L*4, 601 nm, and *L*3, 673 nm) which corresponds with results noted below where West Spur spectra have the most negative 601 nm band depths (most convex spectra at 601 nm). Negative 535 nm band depth values are associated with the targets Assemblee (viewed on sol 575) and Wende (viewed on sol 629) and these show up in Figure 5 as high factor values associated with band 3 (e.g., *L*5, 535 nm). Samples with extreme values along the projection toward band 1 (*L*7, 432 nm) are Wishbone (viewed on sol 332) and Wishstone (viewed on sol 337). Examination of these spectra do not indicate anomalously high 432 nm *R** values; however, Wishstone class spectra were given as one of the six classes with unique spectra by *Farrand et al.* [2006] and thus are included as a candidate class here. Samples with maximum values in factor 6 (not shown as a figure) are associated with Plains Basalt-type spectra and samples with minimum values are associated with Jibsheet class spectra. The

Table 5. Correspondence Analysis Results

	Minimum	Maximum
Factor 1	a386 near Alligator p2546, a269 unnamed rock 2 p2534, and a269 unnamed rock 3 p2534	a381 Peace RAT 1 p2543, a381 Peace RAT 2 p2543, and a63 basalt 1 p2532
Factor 2	a689 Wolf Lake p2568, a690 Iroquet RAT brushed p2575, and a690 Iroquet bare p2575	a220 type 2 p2565 and a419 Watchtower RATed p2574
Factor 3	a663 Lovegrass 2 p2532 and a764 Stars RAT brushed p2589	a879 layers p2265, a754 Barnhill p2584, and a748 layers p2579
Factor 4	a381 Peace RAT 1 p2543 and a60 Humphrey RATed	a536 Independence p2540 and a532 Independence p2532
Factor 5	a210 Pico p2561, a220 Pico p2565, and a227 Frio p2572	a572 Assemblee p2541, a200 Wooly Patch scuffed p2556, and a200 Sabre p2556
Factor 6	a503 Moby p2550 and a487 Davis 2 p2531	a773 vesicular basalt p2456 and a41 basalt 2 p2532

Table 6a. Unnormed Potential Classes Determined by SMACC

Unnormed Spectra	Candidate Class Association	Unique 0.05 Threshold	Unique 0.06 Threshold
a386 near Alligator undisturbed p2546	Methuselah	X	X
a381 Peace RATed 2 p2543	Peace	X	X
a220 unnamed rock p2565	Watchtower	X	X
a690 Iroquet RAT brushed p2575	Seminole	X	X
a269 unnamed rock p2534	West Spur		
a534 Missile p2536	Backstay	X	X
a200 Wooly Patch scuffed p2556	Methuselah	X	
a608 outcrop 2 p2583	Jibsheet	X	
a641 Shaunee p2589	Methuselah	X	
a381 Peace RATed 1 p2543	Peace		
a536 Independence p2540	Independence	X	X
a430 Boddington p2594	Methuselah		
a483 Yardarm p2590	Methuselah	X	
a227 Frio p2572	West Spur		
a419 unnamed rock p2574	Watchtower		
a596 Ang Rita p2564	Methuselah		
a546 Paris p2554	Backstay		
a210 Pico p2561	West Spur	X	X
a647 Aster p2568	Methuselah		
a663 Lovegrass 2 p2532	Stars	X	

Jibsheet samples also plot near band 10 ($R5$, 904 nm) in factor space, which could be representative of the shallow 904 nm bands associated with this spectral class.

5.4. Sequential Maximum Angle Convex Cone Classes

[19] Tables 6a and 6b shows rock spectral end-members determined by application of the SMACC algorithm to the 246 spectra database. SMACC was run on both the R^* and the albedo-normalized R^* data and results from both of these runs are shown, in which the model runs were constrained to select 20 end-members. Choosing a smaller number of end-members would result in the model selecting the same end-members up to that number; a larger number would have resulted in more end-members, which would not be spectrally unique, on the basis of our experimentation with this data set.

[20] The results in Tables 6a and 6b represent raw results for both unnormalized (Table 6a) and albedo-normalized data (Table 6b). The SMACC routine has a means for eliminating redundant choices (i.e., those that are spectrally similar to those already chosen). This filter was turned off for the runs reported in the first columns of Tables 6a and 6b, but was then turned on in order to gauge how many classes were spectrally "unique." The filtering mechanism for determining spectrally unique end-members consists of the application of a spectral angle metric to each end-member spectrum chosen after the first. As was discussed above, two spectra that have a low spectral angle are spectrally similar. For the test in the filtering mechanism of the SMACC approach, spectral angle thresholds of 0.05 and 0.06 radians were used. Thus, in the first case, if the spectral angle between two spectra was greater than 0.05 then they would be deemed dissimilar enough for the newly selected spectrum to be included as a "nonredundant" end-member. These tests are represented in Tables 6a and 6b by the third and fourth columns. It is worth noting that even though a newly selected end-member spectrum might be rejected as "nonunique, "it nonetheless could potentially be

Table 6b. Normed Potential Classes Determined by SMACC

Normed Spectra	Candidate Class Association	Unique 0.05 Threshold	Unique 0.06 Threshold
a664 bare rock p2535	Seminole	X	X
a381 Peace RATed 1 p2543	Peace	X	X
a220 p2565 type 2	Watchtower	X	X
a695 Comanche p2584	Comanche	X	X
a689 Wolf Lake p2568	Seminole	X	X
a764 Stars RAT brush p2589	Stars	X	X
a269 Palenque p2534	West Spur	X	
a663 Lovegrass 2 p2532	Stars	X	X
a687 Lac p2561	Seminole		
a200 Wooly Patch scuffed p2556	Methuselah		
a416 Sentinel p2567	Watchtower		
a41 Sarah p2530	Plains Basalts		
a210 Pico p2561	West Spur	X	
a90 Basketball p2535	Plains Basalts	X	X
a749 Radcliffe p2580	Posey		
a236 Ebenezer RATed p2580	West Spur		
a879 Layers	Posey		
a551 Descartes p2558	Descartes		
a641 Shaunee p2589	Methuselah		
a555 Guillotine matrix p2576	Plains Basalt		

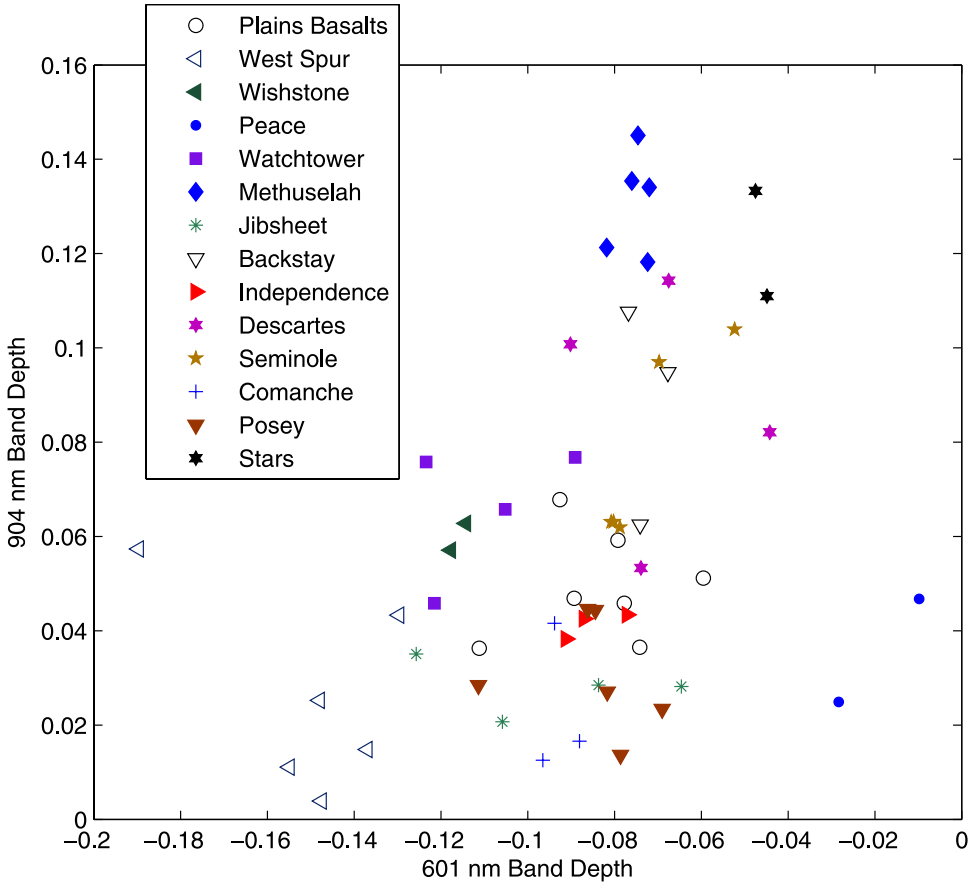

Figure 6. The 601 versus 904 nm band depth for all 14 candidate classes.

more spectrally representative of a class than one of the initially selected unique spectra.

[21] Following the approach of "filtering" end-members, 7 end-members were selected from the unnormed set of spectra using a 0.06 rad threshold and 12 were selected using a 0.05 rad threshold. For the normed spectra, 8 end-members were selected using the 0.06 and 10 using the 0.05 rad threshold. On the basis of these results, between 7 and 12 unique spectral types were indicated. This result was consistent with an earlier result in which a set of spectral classes were determined on the basis of visual inspection of spectra and with an earlier iteration of PCA [*Farrand et al.*, 2007]. Candidate classes from Table 3 are associated with these SMACC-identified spectra in column two of Tables 6a and 6b.

5.5. Examination of Spectral Parameters/Spectral Classes

[22] From the PCA, CA, and SMACC analyses, along with visual inspection of rock spectra and previous work [*Farrand et al.*, 2006, 2007], the 14 candidate spectral classes listed in Table 3 and shown in Figure 2 were determined. While there is variability within these classes, each has spectral features that define them. Spectral parameters listed in Table 2 can be used to further quantify the distinctive features of these spectra. In Figure 6 we present a plot of 601 nm band depth versus 904 nm band depth with all 14 candidate spectral classes. As Figure 6 illustrates, plotting parameters from representative spectra from all 14 candidate classes makes such plots more difficult to interpret. So in the spectral parameter plots in Figures 7–11, we plot only those classes with extreme values of one or more of the plotted parameters. The one exception is that on these plots we also include representative points from the spectral class that we refer to here as "Plains Basalts." These rocks, exemplified by those examined on the Gusev Plains such as Humphrey, but also outliers observed in the Columbia Hills such as Cricket and vesicular basalts observed in the vicinity of Home Plate, have been identified as basalts on the basis of APXS chemistry, MB and Mini-TES determined mineralogy and visual observation with Pancam and MI [*McSween et al.*, 2006a, 2008]. This class is geologically important since basalt is a more familiar rock type than the clastic rocks examined over most of the Columbia Hills traverse and thus is valuable for inclusion in spectral parameter plots for comparison against other classes. We henceforth refer to those classes included in the spectral parameter plots of Figures 7–11, as "primary" classes and to the remaining candidate classes, which have spectral features similar to primary classes, as "subclasses." Table 7 lists the primary classes and their defining spectral characteristics. Figure 12 shows L357 (left eye bands centered on 673, 535, and 432 nm) composite images of representatives of these classes.

[23] Table 8 lists subclasses, their defining spectral characteristics and the primary class that they most closely resemble. Both the primary and subclasses are named either

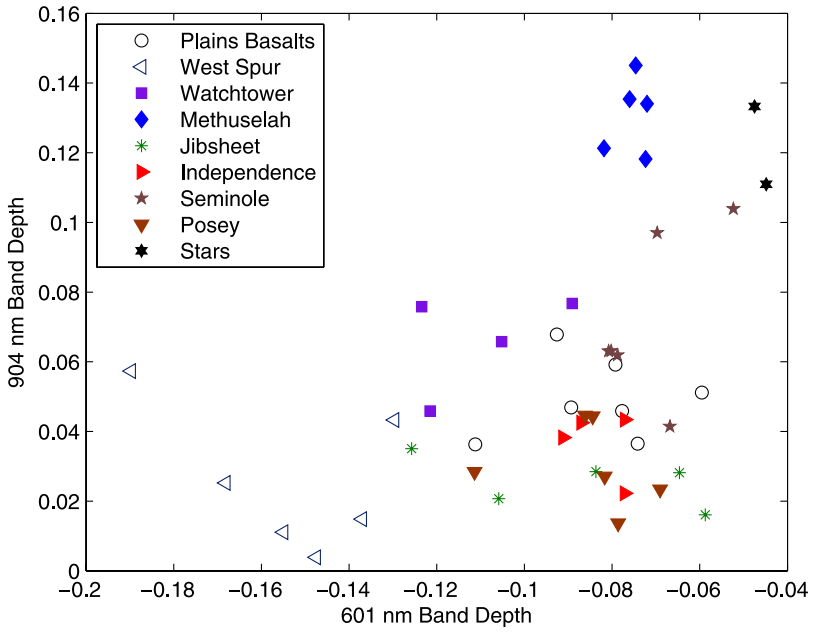

Figure 7. The 601 versus 904 nm band depth for primary spectral classes.

after exemplar spectra that represent the class, after regions from which the rocks displaying these spectral shapes were primarily found, or to connect them with an equivalent chemical class [*Squyres et al.*, 2006]. Figure 13 compares subclass "exemplar" spectra with the associated primary class exemplar spectrum.

[24] The spectral parameter plots shown in Figures 7–11 illustrate distinctive features of the primary spectral classes listed in Table 7. Parameters from several representative spectra from each class are plotted in order to provide a measure of within class variability. Two to three spectra from each class are also plotted in Figure 14 to further illustrate this within class variability. Table 9 lists the sol number, target name (if any, some are unnamed rocks within scenes), and sequence ID for spectra used in the spectral parameter plots.

5.6. Mapping Rock Spectral Classes

[25] Spectral variability between these rock spectral classes is significant enough that representatives of these classes are readily separable in 13 filter images containing more than one spectral class. Examples are shown in Figures 15 and 17. Figure 15 shows the sol 608 P2582 image sequence covering part of the target Tenzing, which can be grouped within the Jibsheet spectral class and other unnamed rocks in the left-hand portion of the scene which have a deeper

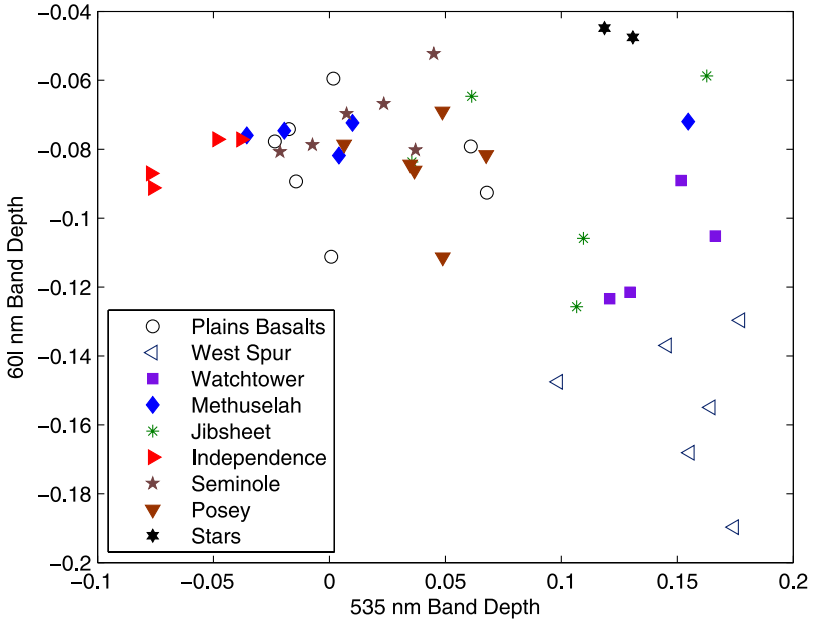

Figure 8. The 535 versus 601 nm band depth for primary spectral classes.

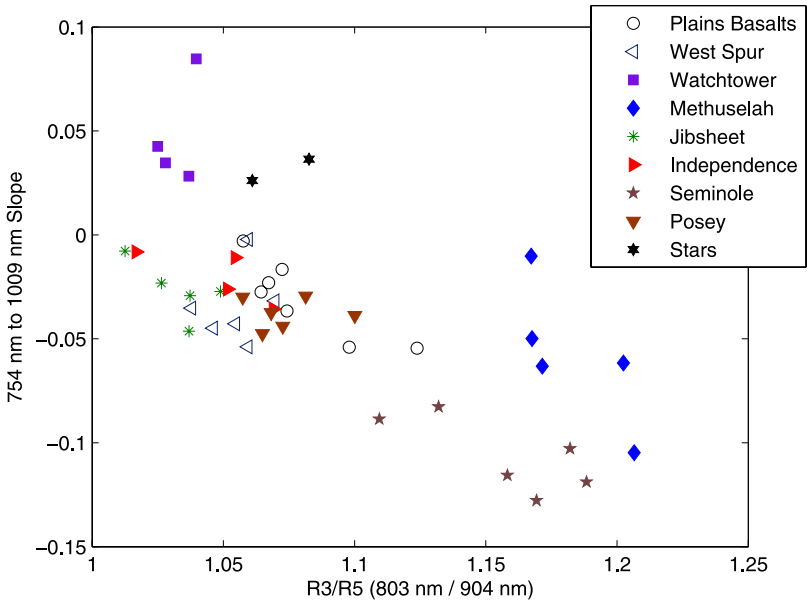

Figure 9. *R3:R5* (803:904 nm) versus 754–1009 nm slope for primary spectral classes.

904 nm band depth and can be grouped within the Methuselah spectral class. The separability of these classes is demonstrated in Figure 15b which graphically shows the differences in 904 nm band depth between the representatives of the Jibsheet and Methuselah spectral classes and in Figure 15c which is a composite of fraction images derived from application of constrained energy minimization (CEM) [*Farrand and Harsanyi*, 1997] to the right eye scene using target spectra for the Methuselah spectral class, Tenzing (Jibsheet class), and bright drift. Figure 16 shows the spectra of the units mapped in the composite image in Figure 15c.

[26] Figure 17 shows the sol 659 P2587 scene in similar portrayals. This includes the feature "Larry's Bench" which was one of the first recognized examples of Seminole class rocks. The scene includes rocks with spectra that can be grouped with the Methuselah class as well as those from the Seminole class. Figure 18 shows the spectra of the units mapped in the CEM fraction composite of Figure 17b.

6. Discussion

6.1. Relevance of Spectral Characteristics to Observations From Other Athena Instruments

[27] The characteristic spectral parameters of the spectral classes determined here have relevance for their composition and/or mineralogy, and these characteristics can be compared with results from other instruments in the Athena

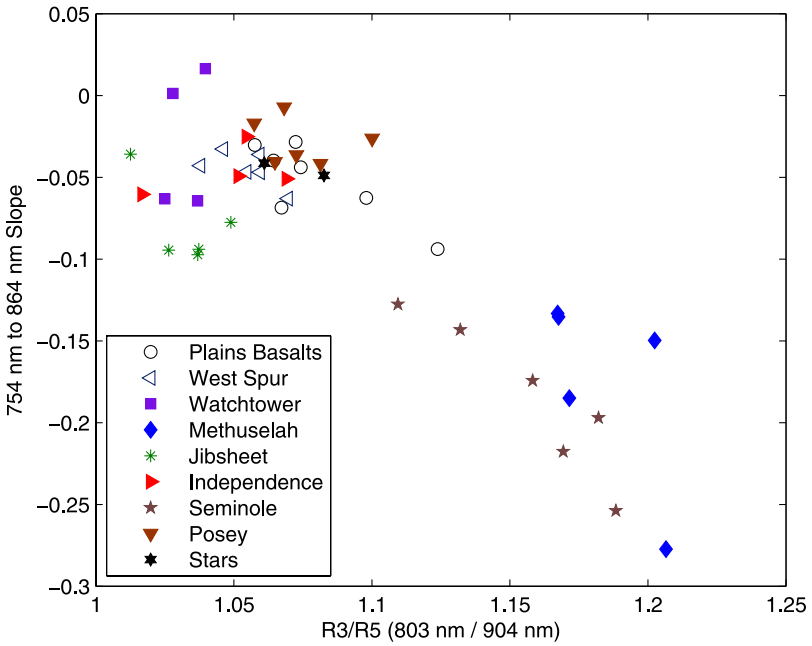

Figure 10. *R3:R5* (803:904 nm) versus 754–864 nm slope for primary spectral classes.

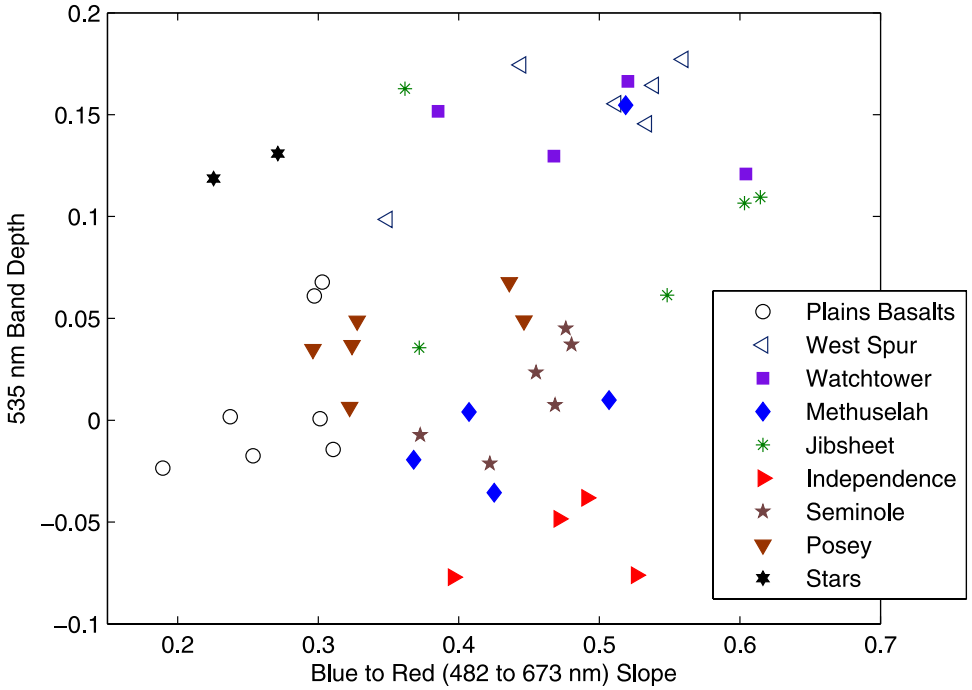

Figure 11. Blue to red slope (482–673 nm slope) versus 535 nm band depth for primary classes.

science payload. As noted above, the West Spur rocks have the highest 535 nm band depths and most negative 601 nm "band depths." The Watchtower rocks also plot very close to the West Spur rocks in plots of these parameters. Nevertheless, some Jibsheet rocks considered here and some of the Posey class and the Stars RAT brush spots also have relatively high 535 nm band depth values (>0.08). Interestingly, no other set of rocks encountered through the period considered in this paper have had values as high in these spectral parameters.

Table 7. Primary Spectral Classes of Clastic Texture Rocks and Their Distinguishing Spectral Characteristics

Spectral Classes	Distinguishing Spectral Parameters
Plains Basalts	Low 535 nm band depth, low to intermediate 904 nm band depth, relative reflectance maximum at 673 nm (can be subequal with 754 nm reflectance), and low albedo
West Spur	Deepest 535 nm band depths (generally >0.1), most negative 600 nm band depths (<−0.12), negative NIR slope, and shallow 754–864 nm slope
Watchtower	Positive 754–1009 nm slope, positive 934–1009 nm slope, strongly negative 600 nm band depths (<−0.08), and high 535 nm band depths (>0.1)
Methuselah	Strongest 904 nm band depths (generally >0.1), subequal 934–904 nm band minimum, highest 803:904 nm band ratios (>1.15), low 535 nm band depths (<0.05), and 754 nm relative reflectance maximum
Jibsheet	Shallow and broad 900 nm band, steep 482–673 nm slopes, and fairly strongly negative 600 nm band depths
Independence	Lowest 535 nm band depths but moderate blue to red slope, 673 nm relative reflectance maximum, and shallow 900 nm band depths
Seminole	673 nm relative reflectance maximum, high 803:904 nm, negative NIR slope, and 934–1009 nm slope may be negative or positive
Posey	Low albedo, higher 535 nm band depth and blue to red slope than Basalts, low 904 nm band depths, moderately high (less negative) 600 nm band depths, and only mildly negative 754–1009 nm slopes
Stars	Steep 934–1009 nm slope, higher 535 nm band depth than basalts, but equally low blue to red slope, least negative 600 nm band depth, 934 nm band minimum, high 900 nm band depth, positive 754–1009 nm slope, and low albedo

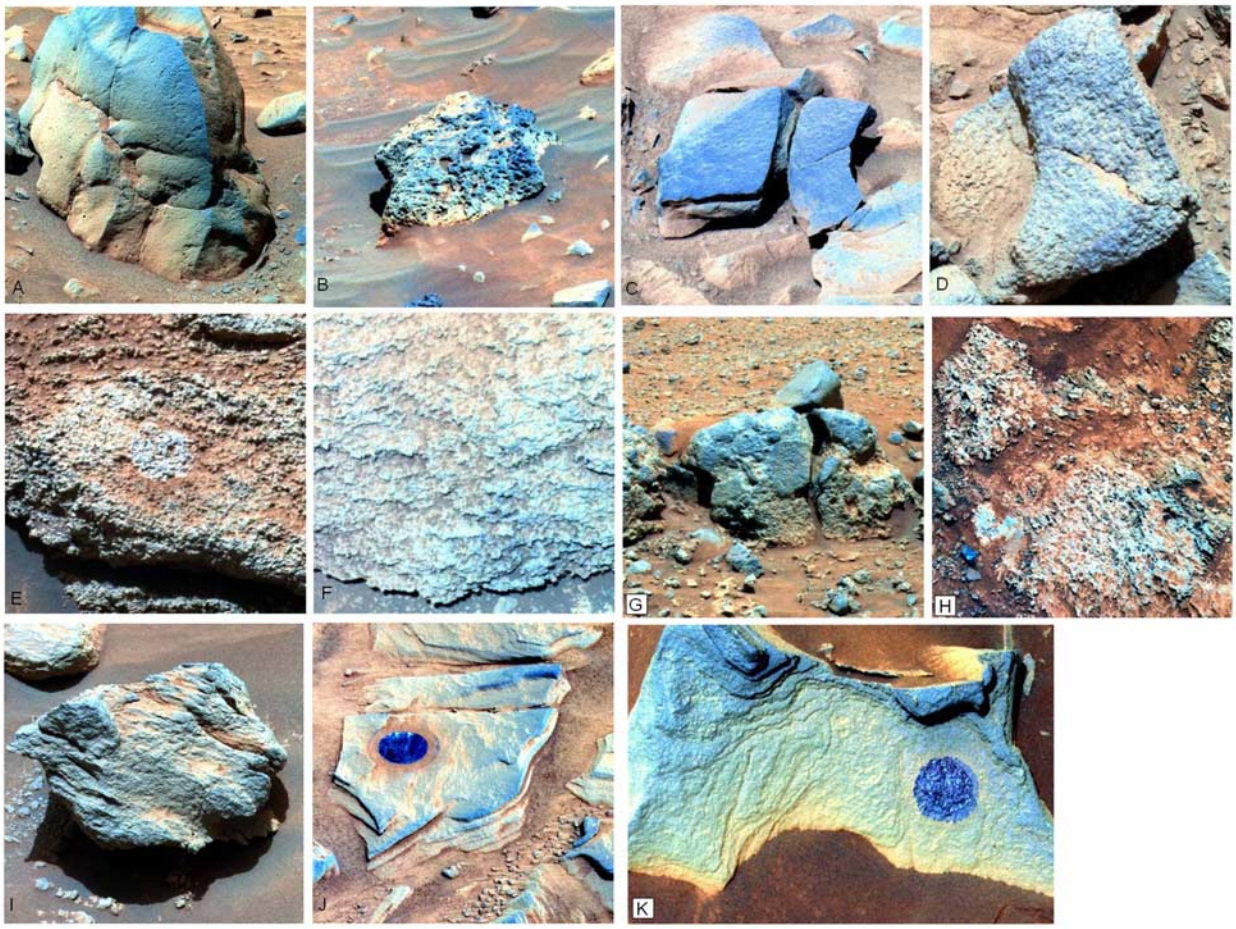

Figure 12. Color composites of representatives of primary rock spectral classes. All images are L357 (673, 535, and 432 nm) composites using a 2% stretch (excluding the minimum and maximum 2% of the data numbers and stretching data values between the remainder). Where a class contains texturally different groups, more than one example is shown. (a) Sol 54 P2429 Humphrey, example of Plains Basalts spectral class. (b) Sol 736 P2566 Cang Jie, example of Plains Basalts spectral class. (c) Sol 227 P2572 Frio, example of West Spur spectral class. (d) Sol 409 P2562 Watchtower, example of Watchtower spectral class. (e) Sol 487 P2531 Davis RAT brush spot, example of Jibsheet spectral class. (f) Sol 470 P2561 Keystone, example of Methuselah spectral class. (g) Sol 647 P2568 Aster, alternate example of Methuselah spectral class. (h) Sol 536 P2540 Independence, example of Independence spectral class. (i) Sol 689 P2568 Wolf Lake, example of Seminole spectral class. (j) Sol 764 P2589 subsection Stars RAT brush spot, example of Stars spectral class. (k) Sol 753 P2583 Posey RAT brush spot, example of Posey spectral class.

[28] It was noted by *Farrand et al.* [2006] that the 535 nm band depth parameter can be related to Fe^{3+}/Fe_{Total} values as determined by the Mössbauer Spectrometer (MB) instrument [*Morris et al.*, 2006]. This point is illustrated in Figure 19 where MB-determined Fe^{3+}/Fe_{Total} versus 535 nm band depth is shown for 15 IDD targets, in which an r^2 correlation of 0.73 is observed. Not plotted are the IDD targets on the rock Independence, which had negative 535 nm band depth values and would plot well below the points in Figure 19. As is noted below, Independence was anomalous with its low total Fe content and negative 535 nm band depths.

[29] The highest values of NIR spectral parameters, such as 904 nm band depth, *R*3:*R*5 (803:904 nm) ratio, and the lowest-NIR spectral slopes (754–864 and 754–1009 nm), are associated with the Methuselah and Seminole primary classes and their associated subclasses (Descartes, Wishstone, and Comanche). Methuselah and Seminole have 803:904 nm ratios greater than 1.14.

[30] Comanche was detected as a candidate class and like the Seminole class spectra, the Comanche spectra have a negative 754–1009 nm slope; however, the relative reflectance maximum of the Comanche spectra is shifted to 754 nm (from 673 nm for the Seminole spectra) and Comanche spectra have a steeper blue to red slope (Figure 13e). These differences accord well with MB results (Table 10) that showed the Seminole class rocks, such as the Iroquet RAT brush, to have very high olivine/pyroxene ratios while the two Comanche IDD spots examined had higher fractions of pyroxene. These iron mineralogy differences help to

Table 8. Spectral Subclasses

Subclass	Most Similar Class	Difference From Primary Class(es)
Peace	Plains Basalts	Shallower (to negative) blue to red slope and no 535 nm band depth
Backstay	Plains Basalt	Positive to low negative 754–1009 nm slope, 673 nm relative reflectance maximum, and 600 nm band depth that is less negative than other basalts
Wishstone	Methuselah	Greater 535 nm band depth, more negative 601 nm band depth, and shallower 900 nm band depth
Descartes	Methuselah	Has 673 nm (instead of 754 nm) relative reflectance maximum, 934 nm band minimum, and shallower blue to red slopes
Comanche	Seminole	Shallower 900 nm band depth, less negative 601 nm band depth, higher 535 nm band depth, and relative reflectance maximum at 754 instead of 673 nm

account for the subtle differences in the Seminole and Comanche class spectra because a greater abundance of pyroxene in Comanche could account for its longer wavelength relative reflectance maximum. Also, MB results (Table 10) indicate a higher Fe^{3+}/Fe_{Total} ratio in the Comanche IDD target than in the Iroquet (Seminole spectral class) IDD target which also supports the Pancam observation of a steeper blue-to-red slope in the Comanche spectra.

[31] The Methuselah spectral class is included here as a collection of spectra from different areas, namely the lower West Spur (characterized primarily by several spectra from the rock Wooly Patch), the namesake Methuselah area on Cumberland Ridge (including the IDD spot Keystone and other targets imaged but not examined in situ such as the Witch and Hag targets), several rocks that were imaged but not examined by the IDD (such as the target Bowline) at the Husband Hill summit, and a number of rocks and outcrops from the Haskin Ridge area (including the IDD spot Kestrel and rocks imaged but not measured by the IDD such as Shaunee and Aster). According to the MB measurements (Table 10 [*Morris et al.*, 2006, 2008]), these areas all have on the order of 30% or more of their iron in pyroxene.

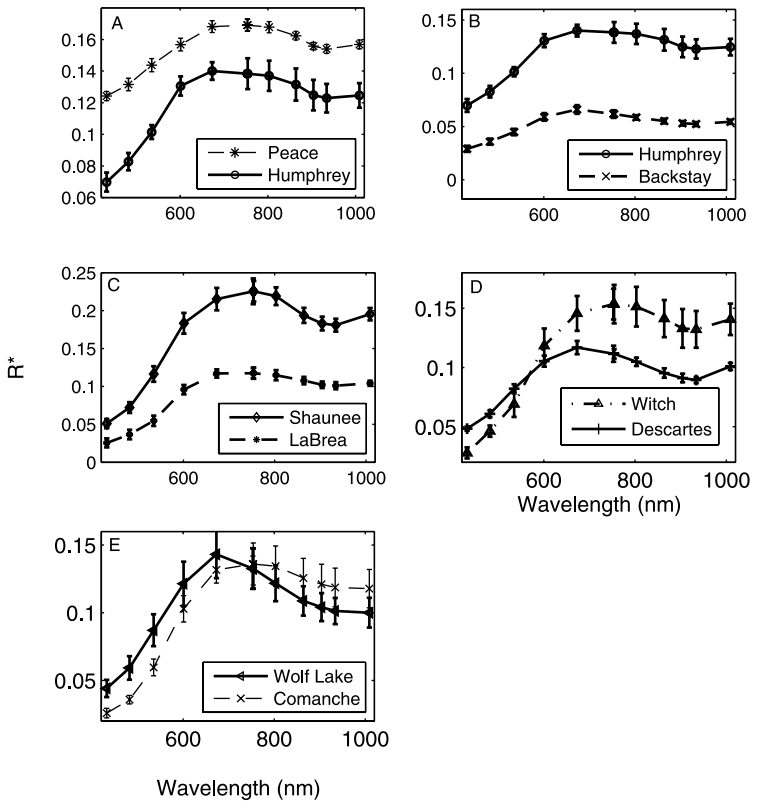

Figure 13. Comparison of primary and subclass spectra. (a) Plains Basalt (represented by a54 Humphrey undisturbed) compared with one of the Peace RAT grind measurement spots. (b) The a54 Humphrey undisturbed compared with the Backstay subclass (represented by a511 Backstay). (c) Methuselah (represented by a641 Shaunee) compared with the Wishstone (represented by a343 LaBrea) subclass. (d) Methuselah (represented by a465 Witch) compared with the Descartes (represented by a551 Descartes) subclass. (e) Seminole (represented by a689 Wolf Lake) compared with the Comanche (represented by a695 Comanche) subclass.

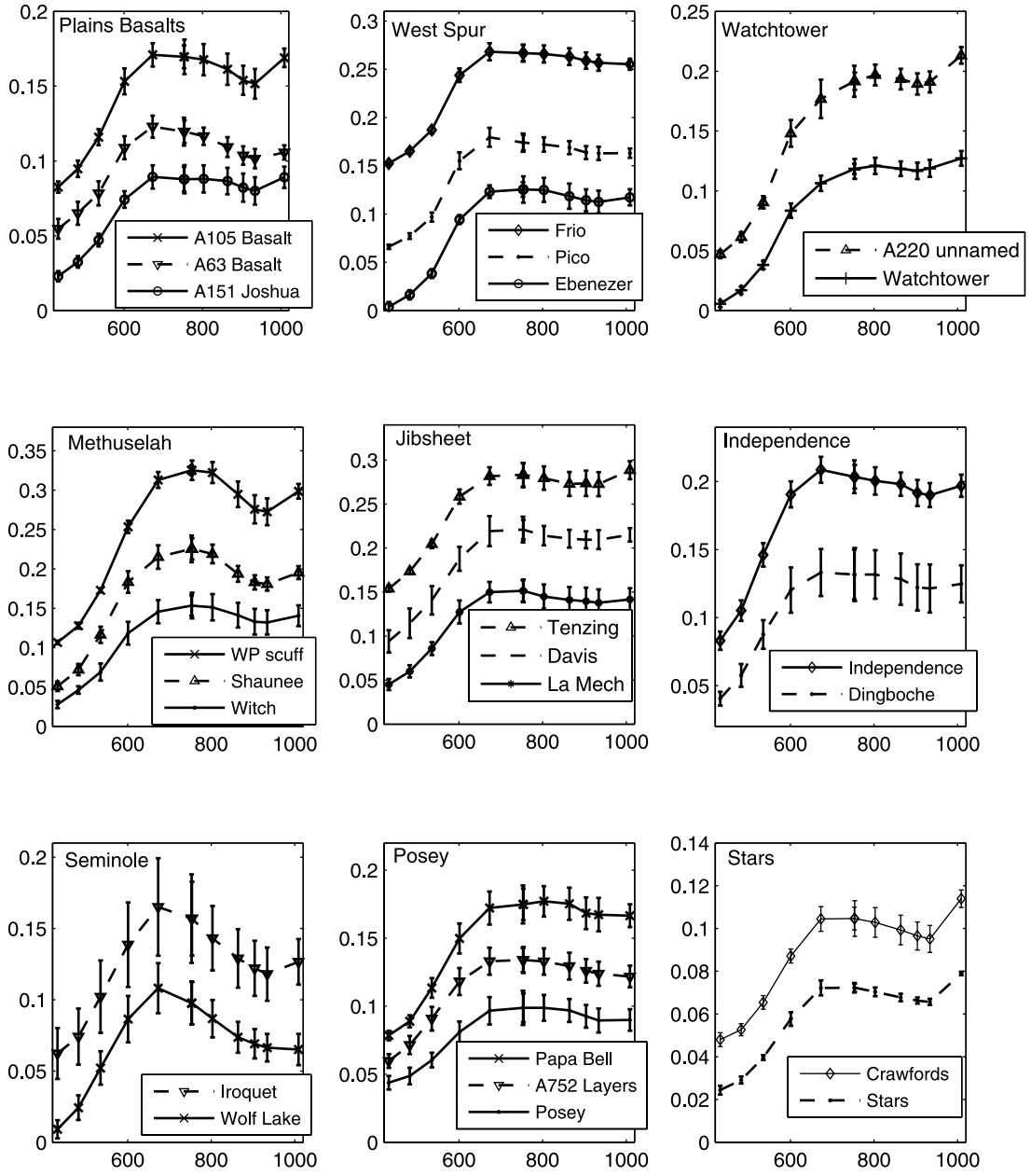

Figure 14. Representative spectra of the nine primary spectral classes.

Kestrel also has a significant fraction of the iron in goethite. These different rock targets have in common low to no olivine, a significant fraction of pyroxene, significant nanophase ferric oxide (npOx) and some (greater than 10%) fraction of hematite and/or goethite. The latter values indicate that these are not pristine rocks (there has been some degree of oxidation/alteration). A mixture of pyroxene and the Fe^{3+} phases can also account for the strong 900–934 nm absorption in the Methuselah spectral class.

[32] It is instructive to also compare the Methuselah spectral class rocks to Methuselah subclasses and also to compare spectra from the different Methuselah locations (lower West Spur, Cumberland Ridge and Haskin Ridge) with each other. Wishstone rock spectra generally resemble Methuselah class spectra (Figure 13c) but have somewhat weaker 904 nm band depths (with associated lower 754–864 nm slope and lower 803:904 nm ratio). Wishstone differs from IDD-examined Methuselah class rocks (Mastodon, Keystone, and Kestrel) in terms of MB-determined iron-bearing minerals in that it has more olivine and about the same, or a smaller, percentage of iron in pyroxene [*Morris et al.*, 2006]. The IDD-examined Methuselah class rocks all also have higher fractions of crystalline Fe^{3+}-bearing minerals (hematite + goethite) than are found in Wishstone or in Descartes. The aggregate effect of more crystalline ferric iron phases plus comparable, or more pyroxene, accounts for the greater 904 nm band depth of the Methuselah class rocks compared to that of Wishstone. The Descartes subclass also has a shallower 904 nm band depth than the Methuselah class examples considered and again, according to MB results, Descartes has a lower percentage of iron in pyroxene + hematite + goethite than

Table 9. Target Spectra Used in Spectral Parameter Plots

Class	Target Name	Sol	Sequence
Plains Basalts	Humphrey	54	P2429
	Mazatzal RATed	87	P2530
	Joshua	151	P2586
	Cricket	472	P2566
	Masada	721	P2538
	Luo Zu	736	P2564
	Cang Jie	736	P2566
West Spur	Pico	210	P2561
	Pico	220	P2565
	Unnamed	220	P2565
	Ebenezer	227	P2571
	Frio	227	P2572
	Ebenezer RATed	236	P2580
Wishstone	Wishbone	332	P2563
	Wishstone RATed	337	P2569
	La Brea	343	P2574
Peace	Peace RATed (two spots)	381	P2543
Watchtower	Unnamed	220	P2565
	Lighthouse	414	P2564
	Sentinel	416	P2567
	Watchtower RATed	419	P2574
Jibsheet	La Mech	472	P2564
	La Mech Jr.	474	P2570
	Davis RATed	487	P2531
	Aurora	493	P2537
Methuselah	Wooly Patch scuffed	200	P2556
	Bowline	615	P2590
	Aster	647	P2568
	Unnamed (two rocks)	659	P2587
Backstay	Backstay	509	P2559
	Backstay (two spots)	511	P2563
	Irvine	603	P2577
Independence	Independence	536	P2540
	Dingboche	626	P2536
	Wende	629	P2540
Descartes	Morris	539	P2544
	Descartes	551	P2558
	Fraternite	553	P2564
	Descartes	568	P2533
Seminole	Goldenrod	658	P2585
	Eagle Village	688	P2565
	Wolf Lake	689	P2568
	Iroquet RAT brush	690	P2575
	Iroquet bare	690	P2575
Comanche	Comanche	695	P2584
	Comanche	699	P2591
	Comanche	701	P2597
Posey	Unnamed patch on layers	752	P2581
	Unnamed patch on layers	762	P2588
	Cool Papa Bell	764	P2589
	Unnamed patch on layers	770	P2591
	Unnamed patch on layers	771	P2594
	Unnamed patch on layers	772	P2595
Stars	Lovegrass	663	P2532
	Stars RAT brush	764	P2589
	Crawfords RAT brush	764	P2589

is present in the Methuselah class examples. This effect is graphically depicted in bar graph form in Figure 20 which shows the percentage of pyroxene + hematite + goethite for Methuselah class examples from the three IDD-examined locations mentioned above plus Wishstone and Descartes. On the same bar graph are scaled values of 904 nm band depth and, as stated in this paragraph, it can be seen that the Methuselah class proper examples have higher 904 nm band depth values than the Wishstone and Descartes IDD locations.

[33] Examples of the Jibsheet spectral class include spectra from primarily two areas: the Cumberland Ridge area (rocks such as Davis and LaMech) and from the Husband Hill summit area (rocks such as Tenzing and Edmund Hillary). This spectral class is characterized by a broader, shallower NIR absorption feature. In the spectral parameter plots, the Jibsheet examples are very distinct from the Methuselah spectral class with lower 904 nm band depths, lower $R3{:}R5$ ratios, and shallower 754–864 nm slopes. There were several IDD examinations of rocks with Jibsheet spectral class type spectra. These include Keel and Edmund Hillary. On the basis of the MB results shown in Table 10 the Jibsheet rocks have significantly lower percentages of pyroxene than do the Methuselah spectral class rocks, which accords well with the lower values of the NIR spectral parameters just cited.

[34] The rock Independence had very low amounts of Fe according to in situ examination by the APXS [*Clark et al.*, 2007]. Spectra from this rock were similar to several rocks (e.g., Wende, Dingboche, and Bruce) at the Husband Hill summit that were not examined with the IDD instruments. As was noted above, the Independence examples plotted in Figures 7–11 form a distinct cluster with negative 535 nm band depths and intermediate blue to red (482–673 nm) slopes (Figure 11) and in other plots have low values related to the strength of a NIR absorption feature (e.g., Figure 7). MB results (Table 10) from two IDD targets on Independence indicate relatively high fractions of npOx [*Morris et al.*, 2006]. Even though Independence contained very little iron, what iron phases were present would tend to dominate the VNIR reflectance due to the fact that such phases are the primary ones with spectral features in this wavelength range. The high fractions of npOx in Independence illustrates that higher amounts of npOx do not necessarily correspond to higher 535 nm band depths. The latter spectral parameter is instead related to the incipient (or more advanced) development of hematite, or other crystalline ferric iron phases [*Morris et al.*, 1989; *Bell et al.*, 1993]. Clearly, given the low (negative) 535 nm band depths, there has not been this development of crystalline ferric iron phases for Independence spectral class rocks.

[35] Some indirect supporting evidence for the presence of poorly crystalline materials in Independence comes from observations of this rock by the APXS, Mini-TES, and MB instruments. On the basis of results from the former, *Clark et al.* [2007] concluded that Independence contained montmorillonite or its compositional precursor. Mini-TES did not detect the presence of montmorillonite and those results were more consistent with the presence of an amorphous mineralogy over a crystalline clay mineralogy [*Clark et al.*, 2007]. Likewise, MB results indicated the presence of a significant fraction of poorly crystalline nanophase ferric oxide.

[36] Pancam spectral observations of the Home Plate area are the subject of a more dedicated investigation [*Farrand et al.*, 2008; *Schröder et al.*, 2008; M. E. Schmidt et al., Spectral, mineralogical, and geochemical variations across Home Plate, Gusev Crater, Mars: Evidence for high and low temperature alteration, submitted to *Earth and Planetary Science Letters*, 2008]; however, in summary, two spectral classes were observed in RAT brush spots from the initial investigations near the northwest rim of Home Plate and these are the Posey and Stars spectral classes. The Stars spectral class displays a relatively strong NIR absorption

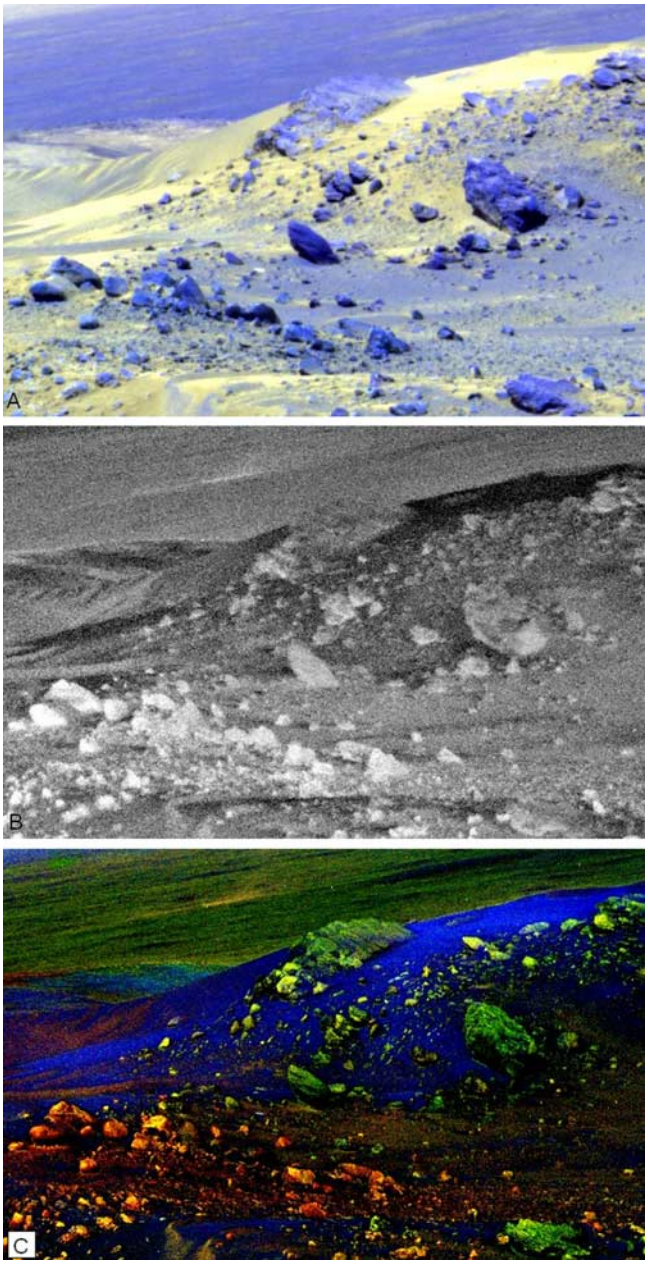

Figure 15. Sol 608 P2582 sequence with representatives of the Jibsheet and Methuselah spectral classes observed near the summit of Husband Hill. (a) R521 (904, 754, and 436 nm) composite. (b) The 900 nm band depth image. (c) Composite of CEM fraction images, where red is the Methuselah spectral class, green is the Jibsheet spectral class, and blue is bright drift.

band (904 nm band depth >0.1) and also has a relatively strong (>0.1) 535 nm band depth. Posey class spectra have similar 535 nm band depth values (Figure 8) but have a much more shallow 904 nm band depth (Figure 7). While not considered further here, the 535 nm band depth, and also the 601 nm band depth values of Posey and Stars class observations from the northwestern portion of Home Plate contrasts with more recent observations of RAT brush spots from the eastern rim of Home Plate (e.g., the sol 1210 observations of Pesapallo and sol 1220 observations of several targets including Elizabeth Emery, Mildred Deegan, and June Stoll) which have lower 535 nm band depth values [*Farrand et al.*, 2008]. The differences between the Posey and Stars spectra are manifested primarily in the 935–1009 nm slope (note that the representatives of these classes also have similar 754–864 nm slope values in Figure 10). The MB results (Table 10) also indicate very similar Fe-bearing mineralogies between Posey and Stars representatives. Thus the differences between the 935 and 1009 nm slope values of the two classes might be dictated by thin coatings on the Posey class surfaces. Thin dust coatings have, in laboratory investigations, been shown to produce negative NIR continua and suppress the depth of absorption features [*Fischer and Pieters*, 1993; *Johnson and Grundy*, 2001]. Another possibility is that the Posey class surfaces have a thin coating similar in nature to that observed on the plains basalt Mazatzal [e.g., *Yen et al.*, 2005] with elevated Cl, while no such enrichment was observed on the Posey IDD location, recent examination of the Chanute target on the northern slope of Home Plate have indicated a moderate Cl enrichment.

[37] The Plains Basalts and Backstay spectral class basalts have low (generally <0.02) 535 nm band depths (indicative of minimal oxidation) and differ mainly in the strength and shape of the NIR absorption feature. As can be seen in Figures 6 and 13b, the Plains Basalts and Backstay class basalts have 904 nm band depths greater than 0.03, with the latter having 904 nm band depths generally greater than 0.06. The NIR absorption of the Backstay spectral class examples appears broader than that of the Plains Basalts; however, their iron mineralogy as indicated by MB measurements are comparable with the exception that the Plains Basalts are generally more olivine rich and also that the pyroxenes in Plains Basalts are high Ca pyroxenes while those in Backstay spectral class rocks (such as Backstay and Irvine) are low-Ca pyroxenes. As was first discussed by *McSween et al.* [2006b], this latter fact helps account for the differences in the shape of the NIR absorption feature. Since the crystal field band centered near

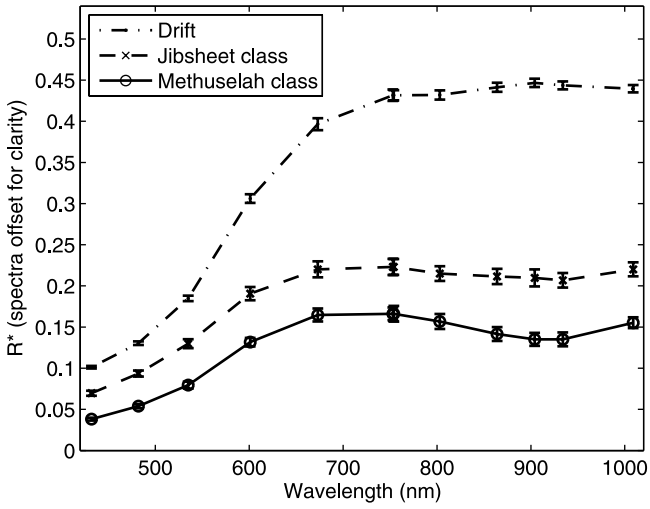

Figure 16. Spectra of the units mapped in Figure 15c. Drift spectrum offset upward by 0.05. Methuselah class offset downward by 0.03.

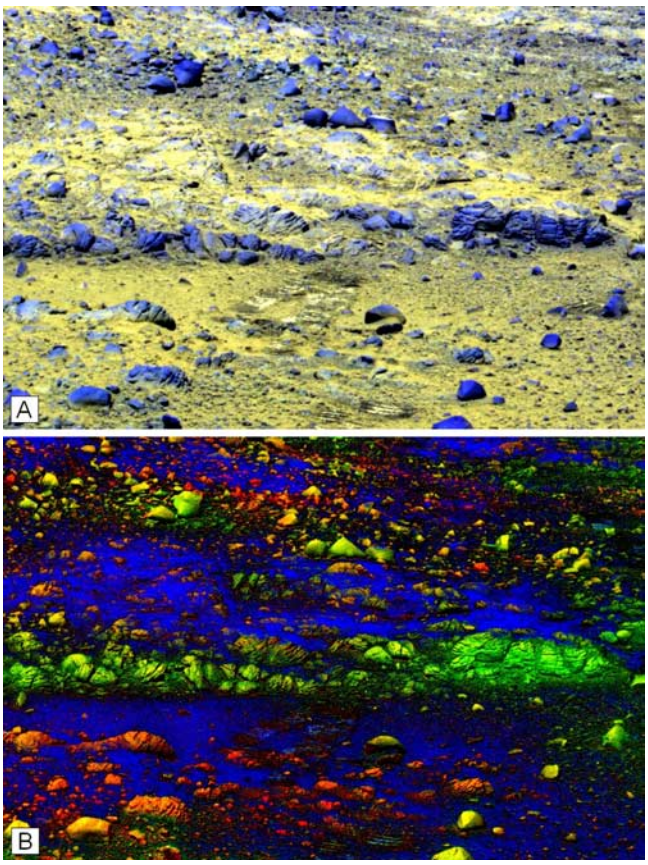

Figure 17. Sol 659 P2587 sequence with representatives of the Methuselah and Seminol spectral classes looking at the Larry's Bench features. (a) R521 (904, 754, and 436 nm) composite. (b) Composite of CEM fraction images, where red is the Methuselah spectral class, green is the Seminole spectral class, and blue is bright drift.

1000 nm occurs closer to, or longward of 1000 nm in high-Ca pyroxenes and closer to 900 nm on low-Ca pyroxenes [*Burns*, 1993] the downturn in reflectance toward that band minimum will occur at a longer wavelength in rocks dominated by high-Ca pyroxenes as opposed to those with mostly low-Ca pyroxenes. This behavior accounts for the appearance of more of a reflectance maximum plateau from roughly 600–800 nm in the Plains Basalts spectra as opposed to the sharper relative reflectance maximum at 673 nm in the Backstay class spectra.

6.2. Relevance of Spectral Characteristics to APXS Rock Classes

[38] As discussed by *Squyres et al.* [2006], the Athena Science Team defines rock classes sensu stricto on the basis of major element chemical analyses, following the convention for volcanic rock classification on Earth. However, other instruments in the Athena Science Payload (e.g., Pancam, Mini-TES, and Mössbauer) may identify distinctive properties within an APXS rock class that require the formation of subclasses that more fully describe the unique properties of a particular rock [e.g., *Morris et al.*, 2006]. Accordingly, certain Pancam spectral classes can fall within a single APXS rock class, indicating a diversity in Pancam spectral properties that is not mirrored by chemistry (e.g., the Watchtower, Methuselah, and Jibsheet spectral classes fall within the Watchtower APXS rock class, Table 3). This is perhaps not a surprising result, as some portion of the Pancam spectral diversity can be attributed to changes in iron redox state that result from processes which impart a minimal imprint on bulk rock geochemistry (e.g., low-water-to-rock ratio aqueous alteration).

[39] We note, however, that Pancam spectral classification can, in some cases, place a particular rock spectra into an APXS rock class to which it bears no chemical resemblance. An example of this is the placement of the scuffed Wooly Patch Pancam spectra into the Methuselah Pancam spectral class (Table 9). In terms of APXS bulk chemistry, analyses of Wooly Patch would properly be placed into the Clovis APXS rock class, whereas occurrences of the Methuselah outcrop at Cumberland Ridge belong to the Watchtower APXS rock class. In this case, the VNIR spectral character of these geochemically and geographically separable rocks is similar enough to warrant their grouping into a single Pancam spectral class. In part, the spectral classes determined from Pancam spectra can thus be more sensitive than APXS to alteration in the form of oxidation of Fe-bearing minerals.

6.3. Comparisons With Mini-TES Rock Spectral Classes

[40] Multispectral observations made in the VNIR with Pancam are supported by hyperspectral thermal infrared (TIR) observation made by Mini-TES. *Ruff et al.* [2006] discussed spectral classes observed up to the examination of the rock Backstay (circa sol 510). Further examinations since that time have revealed additional spectral classes [*Ruff et al.*, 2008]. While we have noted subtle spectral differences here between, for example, the Methuselah, Wishstone, and Descartes spectral classes, there are more distinct differences between these spectral classes on the basis of the higher spectral resolution TIR features resolvable by Mini-TES. Likewise, where we include observations of the Comanche outcrop as a subgroup of the Seminole spectral class, Mini-TES is able to resolve these as distinct spectral classes. Likewise, Mini-TES distin-

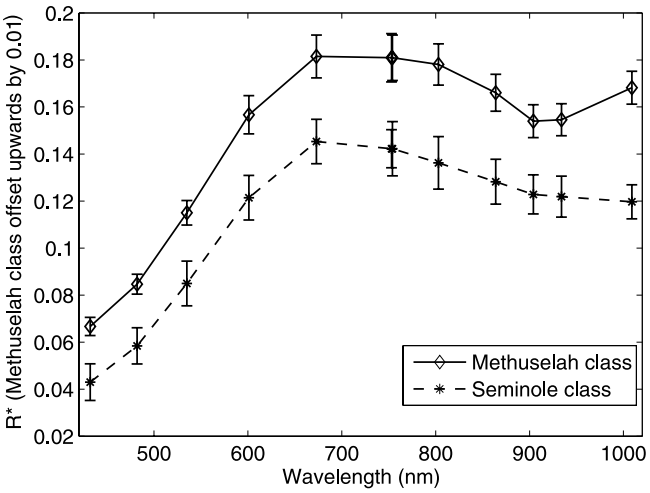

Figure 18. Spectra of the rock classes used as target spectra for the CEM mapping in Figure 17b.

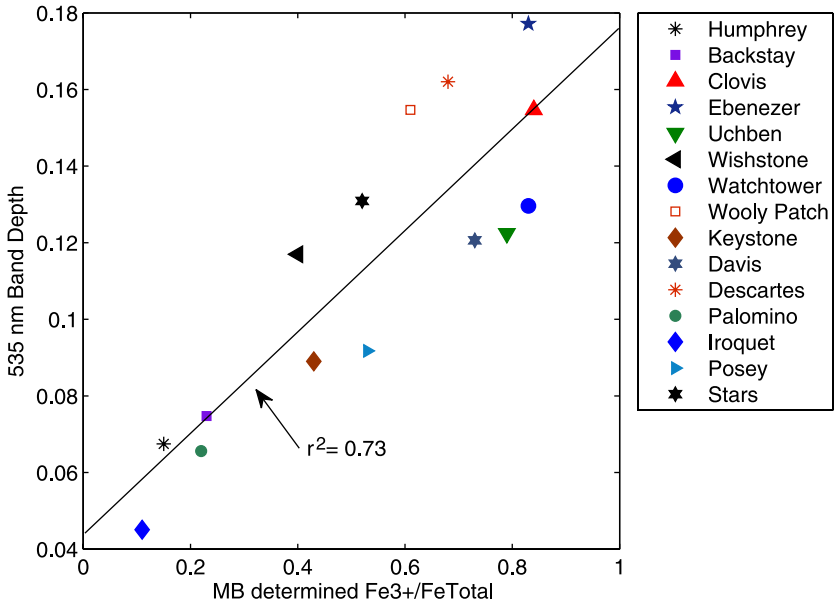

Figure 19. MB determined Fe^{3+}/Fe_{Total} versus 535 nm band depth for a set of 15 representative IDD examined RAT grind or RAT brush spots.

guishes the rock Backstay from Plains Basalts such as Humphrey and Adirondack [*Ruff et al.*, 2006].

6.4. Preliminary Comparisons to Potential Terrestrial Analog Materials

[41] While a detailed comparison of the VNIR reflectance properties of the spectral classes considered here with those of possible terrestrial analog materials is beyond the scope of this paper, we do present here a preliminary comparison made between these spectra from Spirit with library spectra from the CRISM spectral library and basaltic tephra spectra collected by the first author [*Farrand and Singer*, 1992].

[42] Figure 21 shows a 601 nm band depth versus 904 nm band depth plot with the primary spectral classes except for Plains Basalt (IDD analysis have already shown them to be a known lithology, e.g., basalts) but including the Descartes and Comanche subclasses because, as will be seen, these subclasses compare well with some of the analog materials. Among the analog materials plotted are red (on the basis of a red hematite-bearing spectral signature) impact melt rocks from the Manicouagan impact crater [*Morris et al.*, 1995], which plot with West Spur and Watchtower rocks. Highly palagonitized tuffs from the Pavant Butte tuff cone in Utah and the Fort Rock tuff ring in Oregon plot with the Posey spectral class points. Gray basaltic tuffs (partially palagonitized) from Pavant Butte plot away from the various Gusev Crater spectral classes. Gray (not as highly oxidized) impact melt rocks [*Morris et al.*, 1995] plot partially away from the Gusev Crater classes, but have some overlap with the Descartes spectral subclass rocks.

[43] Figure 22 shows a plot of 803:904 nm ratio values versus those for 754–1009 nm slope of the spectral classes and terrestrial analogs. Here the highly oxidized palagonite tuffs and gray basaltic tuffs plot near each other and outside of the field defined by the Posey class points. Red (hematite-rich) impact melt rocks [*Morris et al.*, 1995] plot beyond (with lower 803:904 nm ratios and higher 754–1009 nm slopes) the Watchtower class rocks. This is interpreted as the Manicouagan red impact melt rocks having more crystalline red hematite than is present in the Watchtower rocks; however, it does indicate the higher oxidation level and hematite content in Watchtower spectral class rocks relative to the other Gusev Crater rock spectral classes. Also plotted is a pair of basaltic komatiites from the CRISM spectral library that plot with the Comanche spectral subclass.

[44] Without good analogs are the Methuselah and Seminole spectral class rocks. Examination of the Gusev Crater spectral classes as compared with pure mineral spectra of olivines and pyroxenes from the USGS spectral library [*Clark et al.*, 1993] indicate that the pure pyroxene spectra have higher 904 nm band depths than the Gusev Crater spectral class samples while olivine samples (whose NIR absorption band center is at longer wavelengths beyond 1000 nm) have generally lower 904 nm band depths. Both olivine and pyroxene pure mineral spectra have higher 803:904 nm ratios than the Gusev Crater samples. Thus, the rocks represented by the Methuselah and Seminole spectral classes, while nominally rich in pyroxene and olivine respectively, are not monomineralic (as confirmed by MB measurements) and are thus not well represented by individual spectral library mineral spectra.

6.5. Geologic Implications

[45] A comparison of the distribution of the spectral classes identified here with geologic classes mapped via field geologic mapping techniques [*Crumpler et al.*, 2005] is provided by L. S. Crumpler et al. (Field geologic mapping of the Columbia Hills, Mars, from MER Spirit traverse observations, manuscript in preparation, 2008). Here we provide some observations in this regard, but defer the more comprehensive discussion of geologic implications to that paper. As was noted above, the VNIR spectral classes mapped here accord well with classes mapped via other

Table 10. Summary of Mössbauer Spectrometer Results for Representatives of Spectral Classes[a]

Pancam Spectral Class[b]	MB Target Name[c]	Olivine (%)[d]	Pyroxene (%)	Ilmenite (%)	npOx (%)	Magnetite (%)	Hematite (%)	Goethite (%)	Fe^{3+}/Fe_{Total}
Humphrey	A060 Humphrey Heyworth2 (RAT)	50	32	0	6	11	1	0	0.15
Backstay	A510 Backstay Scuppler (RAT)	35	37	3	13	11	2	0	0.23
Peace	A379 Peace Justice2 (RAT)	24	29	0	14	33	0	0	0.37
West Spur	A218 Clovis Plano (RAT)	1	14	0	25	2	18	40	0.84
	A233 Ebenezer Ratchit2 (RAT)	1	11	0	35	19	14	20	0.83
	A288 Uchben Koolik (RAT)	2	16	0	38	14	8	22	0.79
Wishstone	A336 Wishstone Chisel (RAT)	20	29	8	16	12	14	0	0.40
Watchtower	A418 Watchtower Joker (RAT)	7	7	3	39	1	31	12	0.83
Methuselah	A200 WoolyPatch Mastadon (RAT)	1	33	0	29	16	13	8	0.61
	A472 Keystone Haunch (Brush)	0	47	6	17	10	15	4	0.43
	A648 Kansas Kestrel (Brush)	3	28	9	29	8	0	23	0.59
Jibsheet	A631 Hillary Namchebazaar (Undisturbed)	11	13	11	18	29	17	0	0.54
	A486 Keel Davis (Brush)	4	13	8	27	9	40	0	0.73
Independence	A534 Independence Livingston (Brush)	0	20	24	56	0	0	0	0.56
Descartes	A555 Descartes Discourse (Brush)	1	27	0	43	18	5	7	0.68
Comanche	A702 ComancheSpur Palomino (Brush)	51	27	0	16	1	5	0	0.22
Seminole	A690 Algonquin Iroquet (Brush)	71	13	2	8	6	0	0	0.11
Posey	A754 Posey Manager (Brush)	17	23	0	27	31	3	0	0.53
Stars	A762 JamesCoolPapaBell Stars (Brush)	17	23	0	29	28	3	0	0.52

[a]Results drawn from *Morris et al.* [2006, 2008].
[b]Pancam spectral classes differ in many cases from the rock classes defined on the basis of chemical composition by *McSween et al.* [2006a, 2006b], *Ming et al.* [2006, 2008], *Morris et al.* [2006, 2008], and *Squyres et al.* [2006].
[c]Target name denotes rover (A is Spirit) and sol number of first MB spectrum on target acquired, feature name, target name, and state of target, i.e., RAT is RAT grind, brush is RAT brush, and undisturbed [cf. *Morris et al.*, 2006, 2008].
[d]Percentage of total Fe content associated with particular mineral phase [cf. *Morris et al.*, 2006, 2008].

Athena science instruments. Following conclusions made with those instruments and in other papers [e.g., *Squyres et al.*, 2006; *Crumpler et al.*, 2005], the Gusev Crater plains are dominated by basalts and are younger than the rocks in the Columbia Hills. The field mapping results (Crumpler et al., manuscript in preparation, 2008), on the basis of correlations of mineralogy, outcrop structure and texture, and indicators of bedding and material emplacement mechanism, suggest that there are at least four broad fundamentally different map lithologies that constitute the Columbia

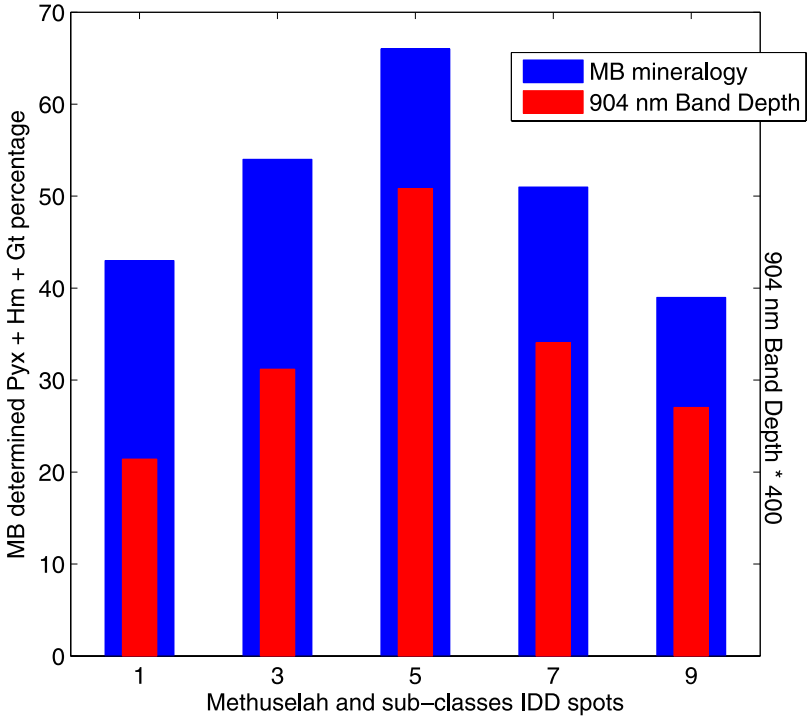

Figure 20. Differences within the Methuselah spectral class and its subclasses. Comparison of scaled 904 nm band depth for RAT grind (Wishstone and Mastodon) and brush (Keystone, Kestrel, and Descartes) spots on the red bar graph (values multiplied by 400) against the cumulative percentage of pyroxene (Pyx), hematite (Hm), and goethite (Gt) on the blue bar graph. Numbers on x-axis represent RAT grind and brush spots: 1 is Wishstone, 2 is Mastodon, 3 is Keystone, 4 is Kestrel, and 5 is Descartes.

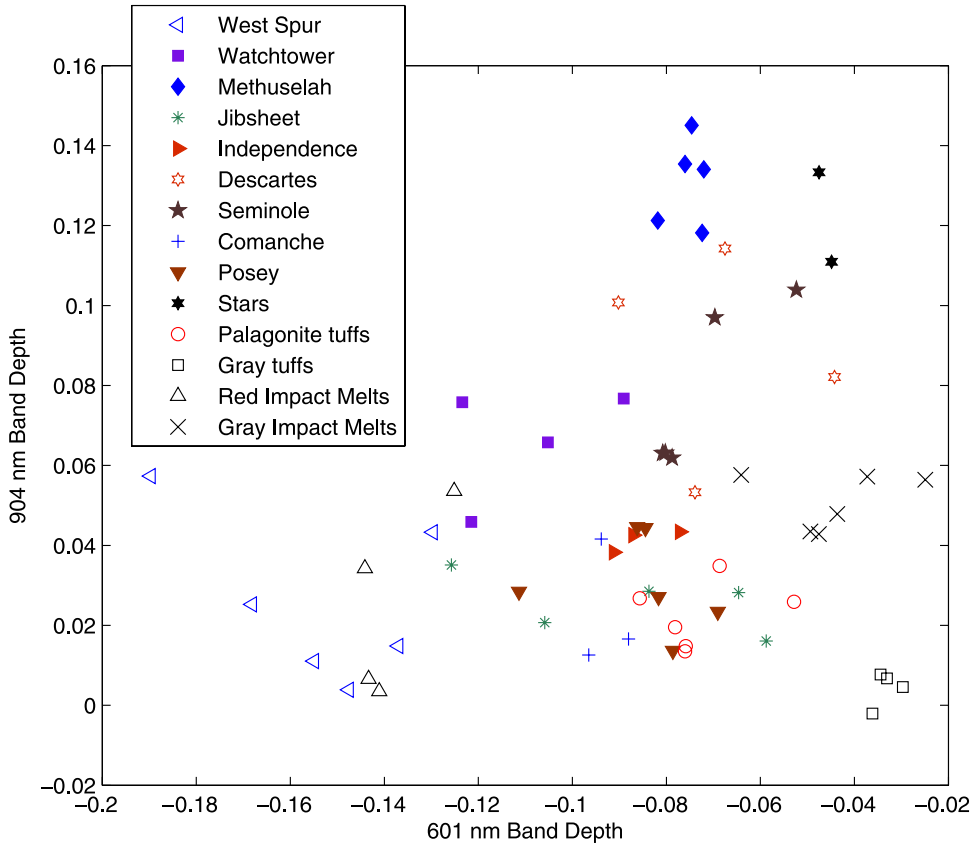

Figure 21. Comparison of 601 versus 904 nm band depth of primary spectral classes excluding Plains Basalt but including Descartes and Comanche subclasses with several potentially analogous terrestrial materials.

Hills. These are defined from field relations rather than mineralogic relations, so these are not strictly correlated with the rock classes defined from chemical and spectral work [*Squyres et al.*, 2006]. In geographic terms, the map lithologies correspond to (1) clastic partially layered units of the West Spur, northwest (Cumberland Ridge), Summit, and east (Haskin Ridge) slopes of Husband Hill; (2) glassy, locally clastic and breccia-like, materials of the west flank of Husband Hill (Independence and Descartes outcrops); (3) the Inner Basin slopes (Algonquin, Comanche); and (4) the Mitcheltree Ridge-Home Plate terrains.

[46] Evidence of increased oxidation, which could be attributed to aqueous alteration, is found in the higher 535 nm band depths and shallowest 601 nm band depths in the rocks on the West Spur and in the Watchtower region on Cumberland Ridge. The high 900 nm band depths and high 803:904 nm ratios of the Methuselah class would be more difficult to interpret absent other information since the occurrences of this spectral class is scattered across several locations in the Columbia Hills. But within these broadly similar units there may be other subtle subdivisions, structures, and complications related to locally variable alteration histories of fundamentally similar protolith materials. But from interpreted overlapping field relationships, the outcrops of the west flank of Husband Hill may constitute the deepest exposures, with the clastic, partially layered and laminated rocks of the West Spur, Northwest slope, Summit, and East Slope of Husband Hill being stratigraphically higher.

[47] The field mapping results (Crumpler et al., manuscript in preparation, 2008) suggest, for example, that while there are several classes of rock defined from APXS results from West Spur (e.g., Clovis) to Cumberland Ridge (e.g., Methuselah) materials along with the Haskin Ridge (e.g., Shaunee), the field relations interpret these as all part of a stratigraphically high sequence of fundamentally air fall (volcanic and impactite) materials bearing local variations in alteration. The spectrally distinct rocks of the Independence and Descartes outcrops (West Flank of Husband Hill) are partial support for the field interpretation that the west flank outcrops represent a different lithology from those on the northwest, summit, and east flanks.

[48] The Seminole spectral class and the associated Comanche subclass have a more uniform distribution occurring only on the south flank of Husband Hill. Although the Seminole outcrop is loosely correlated (on the basis of the field mapping criteria mentioned above) with the upper units like that of the Cumberland Ridge and the Husband Hill summit, their spectral differences from the other outcrops of Husband Hill may relate to the proximity of the distinct and possibly stratigraphically lower Comanche outcrops.

[49] Spectrally, the rocks of Home Plate do not provide any strong evidence for their interpretation as being possible hydrovolcanic surge beds although they provide a distinct spectral map unit which, given better exposures and suffi-

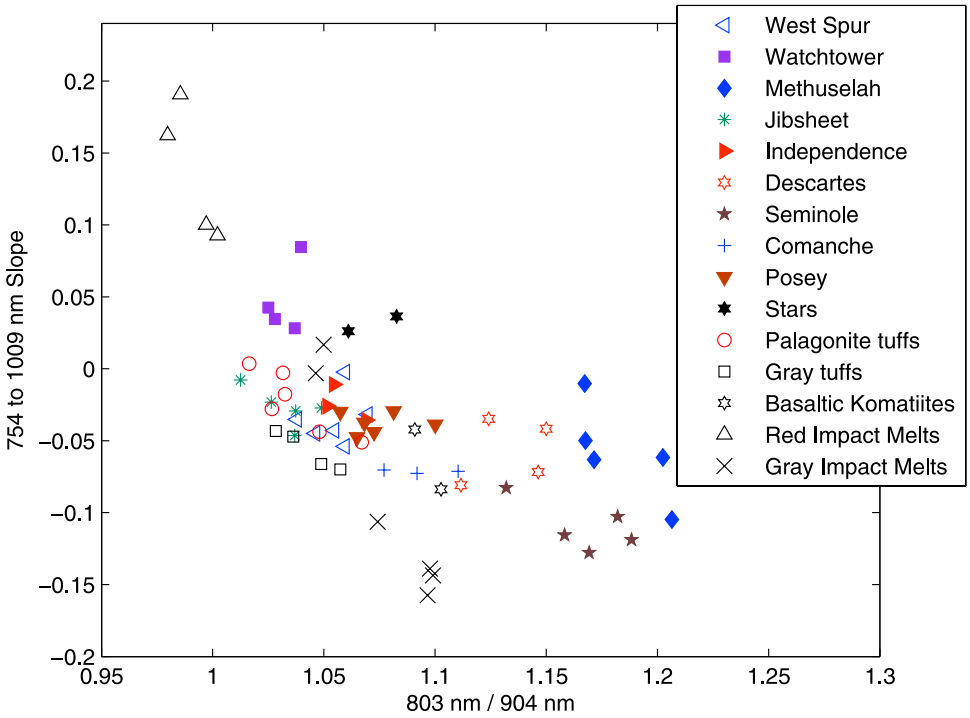

Figure 22. Comparison of 803:904 nm ratio versus 754–1009 nm slope of primary spectral classes excluding Plains Basalt but including Descartes and Comanche subclasses with several potentially analogous terrestrial materials.

cient spatial resolution, might provide information as to the extent of these beds. Also, while soils are not discussed in this paper, associations of these rock spectral units with unique soils mapped by Spirit such as the S-rich Paso Robles type soils [*Wang et al.*, 2008, *Yen et al.*, 2008] and the Si-rich soils near Home Plate [*Squyres et al.*, 2008] could provide additional information as to possible trends in alteration in the Columbia Hills. It is unclear as yet whether bright soils are locally derived from bedrock materials, by air fall, or whether they are recent soils that have drifted and accumulated into current topographic lows, or whether they are exposures of locally deeper sections of the protolith in local topographic lows. In any case they appear to be uncorrelated with local outcrops.

7. Summary and Conclusions

[50] Multispectral measurements in the VNIR by the Spirit rover's Pancam have identified a set of rock spectral classes whose spectral characteristics are indicative of their constituent iron-bearing mineralogy. In this paper, we have combined spectra from the Pancam's left and right eye cameras to assemble a set of 246 spectra gathered from Spirit's landing site on the Gusev Crater plains to its second Winter Haven site in the Inner Basin of the Columbia Hills. 14 candidate spectral classes were determined through analysis of this data set. Analysis techniques used to determine spectrally unique spectra included principal components analysis, correspondence analysis, and a sequential maximum angle convex cone approach. These techniques provided supporting results with spectra representative of the candidate classes repeatedly being selected through the different analysis approaches. Spectral features diagnostic of these classes were examined in greater detail by assessing correlations between spectral parameters drawn from representative spectra.

[51] For the time period considered here (sols 1–800), the most highly altered materials, on the basis of the presence of spectral features indicative of the presence of red hematite and possibly goethite, were the West Spur and Watchtower spectral class rocks which had high 535 nm band depths and were more highly convex (most negative 601 nm band depth) near 600 nm.

[52] The spectra with the deepest 904 nm band depths were the Methuselah spectral class rocks, which included examples from the foot of the West Spur, from Cumberland Ridge, near the Husband Hill summit and on the south flank of Husband Hill on Haskin Ridge. These rocks also exhibited a very negative 754–864 nm slope, but in several instances, especially for the Haskin Ridge examples, had a significant 535 nm band as well, indicating again, the presence of crystalline ferric oxides. These minerals, along with a significant amount of pyroxene (as indicated by in situ measurements with the rover's Mössbauer spectrometer (MB)), account for the deeper 904 nm band in the rocks of this class.

[53] Another class with a highly negative 754–864 nm slope and high 803:904 nm ratio values is the Seminole class, observed on the south flank of Husband Hill. Pancam spectra were able to distinguish between these rocks and the similar Comanche spectral class with the difference between the two being a higher fraction of pyroxene in the latter (again, documented by in situ MB measurements). In the Pancam spectra this difference shows up as a difference in

the position of the relative reflectance maximum for the two classes (673 nm for the Seminole class and 764 nm for the Comanche subclass).

[54] Observations of layered rocks on the Home Plate feature are the subject of other analyses [*Farrand et al.*, 2008; *Schröder et al.*, 2008; Schmidt et al., submitted manuscript, 2008] but in this paper, two spectral classes were observed. MB measurements indicate similar iron-bearing mineralogy for representatives of both, the Posey and Stars spectral classes. These classes are distinguished primarily on the basis of the absence (Posey) or presence (Stars) of a sharp upturn in reflectance from the 935 to 1009 nm (*R6*–*R7*) spectral bands. While the Posey RAT brush observation does not show this upturn in reflectance, most examples of the Posey spectral class that were grouped into the 246 spectra database were of natural surfaces. Given that thin dust coatings can act to produce negative NIR spectral slopes and reduce contrast in spectral features [*Fischer and Pieters*, 1993] it is possible that the primary difference between the surfaces from which these spectra were collected was a thin dust coating on the Posey spectral class surfaces and not on the Stars spectral class surfaces (represented here primarily by the Stars and Crawfords RAT brush spots imaged on sol 764). Another possibility is the presence of a thin, optically translucent cemented coating similar to that observed on the rock Mazatzal [*Yen et al.*, 2005].

[55] A limited set of comparisons with terrestrial analog materials indicates some similarities between the Posey spectral class and palagonitized basaltic tephras. Highly oxidized impact melt rocks from the Manicouagan impact crater have similar spectral parameters (highly negative 601 nm band depth and low 904 nm band depth) to West Spur and Watchtower spectral classes. With regards to the 754–1009 nm slope parameter, these red impact melt measurements are more similar to the Watchtower than to the West Spur class. This is reasonable in light of MB measurements, which indicated that Watchtower rocks had more hematite than did the West Spur class rocks. In the 601 nm band depth versus 904 nm band depth plot, there is also some overlap of the Descartes subclass with ''grey'' Manicouagan impact melt rocks. Some olivine-rich basalt samples have 803:904 nm ratio and 754–1009 nm slope values commensurate with those of the Comanche and some Seminole class rocks.

[56] These Pancam multispectral measurements indicate the utility of VNIR spectroscopy in distinguishing spectral differences between clean (RAT abraded, brushed or eolian abraded) surfaces. These differences reveal a rich lithologic diversity in the Columbia Hills traverse of Spirit. Observations by other instruments in the Athena science package have also noted significant differences in the chemical [*Ming et al.*, 2006, 2008; *Squyres et al.*, 2006], iron mineralogy [*Morris et al.*, 2006, 2008], and thermal IR emittance properties [*Ruff et al.*, 2006] of Columbia Hills rocks. As noted by *Arvidson et al.* [2008] at the 18 m/pixel scale of the orbital CRISM imaging spectrometer, these differences are not observed from existing orbital remote sensing data of the region. Potentially valuable information on lithologic diversity revealed by spectral differences could be obtained by the inclusion of multi to hyperspectral systems either on future rovers or as a component of higher spatial resolution orbital imaging systems.

[57] **Acknowledgments.** Funding for Athena science team members was provided by NASA contracts through Cornell and the Jet Propulsion Laboratory. C.S. acknowledges support by an appointment to the NASA Postdoctoral Program at the Johnson Space Center, administered by Oak Ridge Associated Universities through a contract with NASA.

References

Adams, J. B., M. O. Smith, and A. R. Gillespie (1993), Imaging spectroscopy: Interpretation based on spectral mixture analysis, in *Remote Geochemical Analysis: Elemental and Mineralogical Composition*, edited by C. M. Pieters and P. A. J. Englert, pp. 145–166, Cambridge Univ. Press, New York.

Arvidson, R. E., et al. (2006), Overview of the Spirit Mars Exploration Rover Mission to Gusev Crater: Landing site to Backstay Rock in the Columbia Hills, *J. Geophys. Res.*, *111*, E02S01, doi:10.1029/2005JE002499.

Arvidson, R. E., et al. (2008), Spirit Mars Rover mission to the Columbia Hills, Gusev Crater: Mission overview and selected results from the Cumberland Ridge to Home Plate, *J. Geophys. Res.*, *113*, E12S33, doi:10.1029/2008JE003183.

Bell, J. F., III, R. V. Morris, and J. B. Adams (1993), Thermally altered Palagonitic Tephra: A spectral and process analog to the soils and dust of Mars, *J. Geophys. Res.*, *98*, 3373–3385, doi:10.1029/92JE02367.

Bell, J. F., III, et al. (2003), The Mars Exploration Rover Athena Panoramic Camera (Pancam) investigation, *J. Geophys. Res.*, *108*(E12), 8063, doi:10.1029/2003JE002070.

Bell, J. F., III, J. Joseph, J. N. Sohl-Dickstein, H. M. Arneson, M. J. Johnson, M. T. Lemmon, and D. Savransky (2006), In-flight calibration and performance of the Mars Exploration Rover Panoramic Camera (Pancam) instruments, *J. Geophys. Res.*, *111*, E02S03, doi:10.1029/2005JE002444.

Bell, J. F., III, M. S. Rice, J. R. Johnson, and T. M. Hare (2008), Surface albedo observations at Gusev Crater and Meridiani Planum, Mars, *J. Geophys. Res.*, *113*, E06S18, doi:10.1029/2007JE002976.

Burns, R. G. (1970), *Mineralogical Applications of Crystal Field Theory*, Cambridge Univ. Press, Cambridge, U. K.

Burns, R. G. (1993), Origin of electronic spectra of minerals in the visible to near-infrared region, in *Remote Geochemical Analysis: Elemental and Mineralogical Composition*, edited by C. M. Pieters and P. A. J. Englert, pp. 3–29, Cambridge Univ. Press, New York.

Clark, B. C., III, et al. (2007), Evidence for montmorillonite or its compositional equivalent in Columbia Hills, Mars, *J. Geophys. Res.*, *112*, E06S01, doi:10.1029/2006JE002756.

Clark, R. N., G. A. Swayze, A. Gallagher, T. V. V. King, and W. M. Calvin (1993), The Geological Survey, U. S., Digital Spectral Library: Version 1: 0.2 to 3.0 μm, *Open File Rep. 93–592,* 1340 pp., U. S. Geol. Surv., Reston, Va.

Crumpler, L. S., et al. (2005), Mars Exploration Rover geologic traverse by the Spirit Rover in the plains of Gusev Crater, Mars, *Geology*, *33*, 809–812, doi:10.1130/G21673.1.

Davis, J. C. (1973), *Statistics and Data Analysis in Geology*, 646 pp., John Wiley, New York.

Dennison, P. E., K. Q. Halligan, and D. A. Roberts (2004), A comparison of error metrics and constraints for multiple endmember spectral mixture analysis and spectral angle mapper, *Remote Sens. Environ.*, *93*, 359–367, doi:10.1016/j.rse.2004.07.013.

Farrand, W. H., and J. C. Harsanyi (1997), Mapping the distribution of mine tailings in the Coeur d'Alene River Valley, Idaho through the use of a constrained energy minimization technique, *Remote Sens. Environ.*, *59*, 64–76, doi:10.1016/S0034-4257(96)00080-6.

Farrand, W. H., and R. B. Singer (1992), Alteration of hydrovolcanic basaltic ash: Observations with visible and near-infrared spectrometry, *J. Geophys. Res.*, *97*, 17,393–17,408, doi:10.1029/92JB01075.

Farrand, W. H., J. F. Bell III, J. R. Johnson, S. W. Squyres, J. Soderblom, and D. W. Ming (2006), Spectral variability among rocks in visible and near-infrared multispectral Pancam data collected at Gusev Crater: Examinations using spectral mixture analysis and related techniques, *J. Geophys. Res.*, *111*, E02S15, doi:10.1029/2005JE002495.

Farrand, W. H., J. F. Bell III, J. R. Johnson, and D. L. Blaney (2007), Multispectral reflectance of rocks in the Columbia Hills examined by the Mars Exploration Rover Spirit: Cumberland Ridge to Home Plate, *Lunar and Planet. Sci.*, *XXXVIII*, abstract 1957.

Farrand, W. H., J. R. Johnson, M. Schmidt, and J. F. Bell III (2008), VNIR spectral differences on natural and brushed/wind-abraded surfaces on Home Plate, Gusev Crater, Mars: Spirit Pancam and HiRISE color observations, *Lunar Planet. Sci.*, *XXXIX*, 1774.

Fischer, E. M., and C. M. Pieters (1993), The continuum slope of Mars: Bidirectional reflectance investigations and applications to Olympus Mons, *Icarus*, *102*, 185–202, doi:10.1006/icar.1993.1043.

Gaffey, S. J., L. A. McFadden, and D. B. Nash (1993), Ultraviolet, visible, and near-infrared reflectance spectroscopy: Laboratory spectra of geologic materials, in *Remote Geochemical Analysis: Elemental and Mineralogical Composition*, edited by C. Pieters and P. Englert, pp. 43–71, Cambridge Univ. Press, Cambridge, U. K.

Gellert, R., et al. (2006), Alpha Particle X-Ray Spectrometer (APXS): Results from Gusev Crater and calibration report, *J. Geophys. Res.*, *111*, E02S05, doi:10.1029/2005JE002555.

Gruninger, J., A. J. Ratkowski, and M. L. Hoke (2004), The Sequential Maximum Angle Convex Cone (SMACC) endmember model, in *Proceedings SPIE: Algorithms and Technologies for Multispectral, Hyperspectral and Ultraspectral Imagery X*, vol. 5425, edited by S. S. Shen and P. E. Lewis, pp. 1–14, SPIE, Bellingham, Wash.

Johnson, J. R., and W. M. Grundy (2001), Visible/near-infrared spectra and two-layer modeling of palagonite-coated basalts, *Geophys. Res. Lett.*, *28*, 2101–2104, doi:10.1029/2000GL012669.

Kinch, K. J., J. Sohl-Dickstein, J. F. Bell III, J. R. Johnson, W. Goetz, and G. A. Landis (2007), Dust deposition on the Mars Exploration Rover Panoramic Camera (Pancam) calibration targets, *J. Geophys. Res.*, *112*, E06S03, doi:10.1029/2006JE002807.

Larsen, K. W., R. E. Arvidson, B. L. Jolliff, and B. C. Clark (2000), Correspondence and least squares analyses of soil and rock compositions for the Viking Lander 1 and Pathfinder landing sites, *J. Geophys. Res.*, *105*, 29,207–29,221, doi:10.1029/2000JE001245.

McSween, H. Y., et al. (2006a), Characterization and petrologic interpretation of olivine-rich basalts at Gusev Crater, Mars, *J. Geophys. Res.*, *111*, E02S10, doi:10.1029/2005JE002477.

McSween, H. Y., et al. (2006b), Alkaline volcanic rocks from the Columbia Hills, Gusev Crater, Mars, *J. Geophys. Res.*, *111*, E09S91, doi:10.1029/2006JE002698.

McSween, H. Y., et al. (2008), Mineralogy of volcanic rocks in Gusev Crater, Mars: Reconciling Mössbauer, Alpha Particle X-Ray Spectrometer, and Miniature Thermal Emission Spectrometer spectra, *J. Geophys. Res.*, *113*, E06S04, doi:10.1029/2007JE002970.

Ming, D. W., et al. (2006), Geochemical and mineralogical indicators for aqueous processes in the Columbia Hills of Gusev Crater, Mars, *J. Geophys. Res.*, *111*, E02S12, doi:10.1029/2005JE002560.

Ming, D. W., et al. (2008), Geochemical properties of rocks and soils in Gusev Crater, Mars: Results of the Alpha Particle X-Ray Spectrometer from Cumberland Ridge to Home Plate, *J. Geophys. Res.*, doi:10.1029/2008JE003195, in press.

Morris, R. V., H. V. Lauer Jr., C. A. Lawson, E. K. Gibson Jr., G. A. Nace, and C. Stewart (1985), Spectral and other physicochemical properties of submicron powders of hematite (α-Fe_2O_3), maghemite (γ-Fe_2O_3), magnetite (Fe_3O_4), goethite (α-FeOOH), and lepidocrocite (γ-FeOOH), *J. Geophys. Res.*, *90*, 3126–3144, doi:10.1029/JB090iB04p03126.

Morris, R. V., D. G. Agresti, H. V. Lauer Jr., J. A. Newcomb, T. D. Shelfer, and A. V. Murali (1989), Evidence for pigmentary hematite on Mars based on optical, magnetic, and Mössbauer studies of superparamagnetic (nanocrystalline) hematite, *J. Geophys. Res.*, *94*, 2760–2778, doi:10.1029/JB094iB03p02760.

Morris, R. V., D. C. Golden, J. F. Bell III, and H. V. Lauer Jr. (1995), Hematite, pyroxene, and phyllosilicates on Mars: Implications from oxidized impact melt rocks from Manicouagan Crater, Quebec, Canada, *J. Geophys. Res.*, *100*, 5319–5328, doi:10.1029/94JE01500.

Morris, R. V., et al. (2000), Mineralogy, composition, and alteration of Mars Pathfinder rocks and soils: Evidence from multispectral, elemental, and magnetic data on terrestrial analogue, SNC meteorite, and Pathfinder samples, *J. Geophys. Res.*, *105*, 1757–1817.

Morris, R. V., et al. (2006), Mössbauer mineralogy of rock, soil, and dust at Gusev Crater, Mars: Spirit's journey through weakly altered olivine basalt on the plains and pervasively altered basalt in the Columbia Hills, *J. Geophys. Res.*, *111*, E02S13, doi:10.1029/2005JE002584.

Morris, R. V., et al. (2008), Iron mineralogy and aqueous alteration from Husband Hill through Home Plate at Gusev Crater, Mars: Results from the Mössbauer instrument on the Spirit Mars Exploration Rover, *J. Geophys. Res.*, doi:10.1029/2008JE003201, in press.

Pouch, G. W., and D. J. Campagna (1990), Hyperspherical direction cosine transformation for separation of spectral and illumination information in digital scanner data, *Photogramm. Eng. Remote Sens.*, *56*, 475–479.

Reid, R. J., et al. (1999), Imager for Mars Pathfinder (IMP) image calibration, *J. Geophys. Res.*, *104*, 8907–8926, doi:10.1029/1998JE900011.

Ruff, S. W., P. R. Christensen, D. L. Blaney, W. H. Farrand, J. R. Johnson, J. E. Moersch, S. P. Wright, and S. W. Squyres (2006), The rocks of Gusev Crater as viewed by the Mini-TES instrument, *J. Geophys. Res.*, *111*, E12S18, doi:10.1029/2006JE002747.

Ruff, S. W., P. R. Christensen, T. D. Glotch, D. L. Blaney, J. E. Moersch, and M. B. Wyatt (2008), The mineralogy of Gusev Crater and Meridiani Planum derived from the Miniature Thermal Emission Spectrometers on the Spirit and Opportunity rovers, in *The Martian Surface*, edited by J. F. Bell III, pp. 315–338, Cambridge Univ. Press, New York.

Schröder, C., K. Di, R. V. Morris, G. Klingelhöfer, and R. Li (2008), An east to west mineralogical trend in Mars Exploration Rover Spirit Mössbauer spectra of Home Plate, *Lunar Planet. Sci.*, *XXXIX*, 2153.

Singh, A., and A. Harrison (1985), Standardized principal components, *Int. J. Remote Sens.*, *6*, 883–896, doi:10.1080/01431168508948511.

Sohl-Dickstein, J., J. R. Johnson, W. M. Grundy, E. A. Guinness, T. Graff, M. K. Shepard, R. E. Arvidson, J. F. Bell III, P. R. Christensen, and R. V. Morris (2005), Modeling visible/near-infrared photometric properties of dustfall on a known substrate, *Lunar Planet. Sci.*, *XXXVI*, abstract 2235.

Squyres, S. W., et al. (2003), Athena Mars rover science investigation, *J. Geophys. Res.*, *108*(E12), 8062, doi:10.1029/2003JE002121.

Squyres, S. W., et al. (2006), Rocks of the Columbia Hills, *J. Geophys. Res.*, *111*, E02S11, doi:10.1029/2005JE002562.

Squyres, S. W., et al. (2008), Detection of silica-rich deposits on Mars, *Science*, *320*, 1063–1067, doi:10.1126/science.1155429.

Tian, D., S. Sorooshian, and D. E. Myers (1993), Correspondence analysis with MATLAB, *Comput. Geosci.*, *19*, 1007–1022, doi:10.1016/0098-3004(93)90006-Q.

Wang, A., et al. (2008), Light-toned salty soils and co-existing Si-rich species discovered by the Mars Exploration Rover Spirit in Columbia Hills, *J. Geophys. Res.*, doi:10.1029/2008JE003126, in press.

Yen, A. S., D. W. Ming, R. Gellert, B. C. Clark, R. V. Morris, D. Rodionov, C. Schröder, and G. Klingelhöfer (2005), Subsurface weathering of rocks and soils at Gusev Crater, *Lunar Planet. Sci.*, *XXXVI*, 1571.

Yen, A. S., et al. (2008), Hydrothermal processes at Gusev Crater: An evaluation of Paso Robles class soils, *J. Geophys. Res.*, *113*, E06S10, doi:10.1029/2007JE002978.

R. E. Arvidson, Department of Earth and Planetary Sciences, Washington University, Campus Box 1169, 1 Brookings Drive, St. Louis, MO 63130-4862, USA.

J. F. Bell III, Department of Astronomy, Cornell University, 610 Space Sciences Building, Ithaca, NY 14853, USA.

L. S. Crumpler, New Mexico Museum of Natural History and Science, 1801 Mountain Road NW, Albuquerque, NM 87104, USA.

W. H. Farrand, Space Science Institute, 4750 Walnut Street, Suite 205, Boulder, CO 80301, USA. (farrand@spacescience.org)

J. A. Hurowitz, Jet Propulsion Laboratory, 4800 Oak Grove Drive, Pasadena, CA 91109, USA.

J. R. Johnson, Astrogeology Team, U.S. Geological Survey, 2255 North Gemini Drive, Flagstaff, AZ 86001, USA.

C. Schröder, NASA Johnson Space Center, 2101 NASA Parkway, Houston, TX 77058, USA.